Version of Record: https://www.sciencedirect.com/science/article/pii/S0264817219306294
Manuscript_ba7ca126ec97c860777274c406be0f59

Seafloor depressions on the Nigerian margin: seabed morphology and sub-seabed hydrate distribution

F. Taleb[1], M. Lemaire[2, 3], S. Garziglia[1], T. Marsset[1] and N. Sultan[1]

[1]*IFREMER, Département REM, Unité des Géosciences Marines, F-29280 Plouzané, France*

[2]Université de. Lille, CNRS, UMR 8523 - PhLAM- Physique des Lasers Atomes et Molécules, F-59000 Lille, France

[3]Université de Bordeaux, CNRS UMR 5255 ISM- Institut des Sciences Moléculaires, 33405 Talence, France.

Corresponding author: Farah Taleb (farah.taleb@ifremer.fr)

Highlights:

- Mineralogical analysis is essential if estimating GH content using in-situ data
- 3D scheme of the pockmark and GH occurrence zone created from seismic data
- The geomorphology of the study area is influenced by GH content and distribution

© 2019 published by Elsevier. This manuscript is made available under the CC BY NC user license
https://creativecommons.org/licenses/by-nc/4.0/

Abstract

Gas hydrate quantification using acoustic data requires proper knowledge of the mineralogy of their host sediment. In this paper, a petrophysical model allowing GH quantification at sites where mineralogy profiles are absent is proposed. This approach is applied to a high gas flux pockmark system in the Gulf of Guinea where in-situ acoustic and geotechnical measurements together with core measurements could have been correlated and tied to seismic data. Projections of the in-situ measurements on seismic profiles have shown that the study area not only accommodates zones of shallow and dense GH; but also zones where solid hydrate and free gas coexist as well as pockets of free gas. Further analysis of several seismic profiles has allowed illustrating the detailed GH occurrence zone within the study area, estimate its volume and its occupancy ratio of the pockmark. Correlations between GH content and 3D bathymetry sections have allowed to draw a link between different GH contents and the morphology of the pockmark, which also shares similarities with the morphology of the GH occurrence zone it accommodates.

Keywords: Gas hydrates quantification, Pockmarks, in-situ measurements, seismic profiles, GH distribution, petrophysical model, clayey sediments.

1. Introduction

Gas hydrate (GH) are ice-like solid mixtures of gas molecules, mainly methane, trapped within a crystalline structure of water molecules *(Sloan, 1998)*. These geo-compounds are stable under high pressure and low temperature within a depth range known as the GH stability zone. Their presence also requires continuous supply of gas with a concentration exceeding the solubility limit in water and sufficient amount of water *(Sultan et al., 2010)*. They have been mainly inferred and recovered along continental margins and polar permafrost layers *(Kvenvolden, 1993)*. GH represent the largest stock of natural gas in the world *(Shankar et al., 2013)*, but also a geotechnical hazard threatening offshore operations as well as potential agent of climate change. This made them a target for many scientific and industrial interests.

Understanding the effect of GH on their host sediment behaviour requires knowledge of their physical characteristics, properties, concentration and morphology. *Holland et al. (2008)* showed that the morphology of GH is a means of describing the relation between GH and their bearing sediment as well as defining the physical properties of the sediment-hydrate matrix.

GH are known to be metastable; thus, their identification and characterisation through actual recovery of core samples have been proved challenging *(Dai et al., 2012)*. Therefore, as previously shown by *Sultan et al. (2014; 2010)* and *Taleb et al. (2018)*, in this work the detection of GH has been inferred via in-situ measurements.

These measurements are eventually interpreted using an effective medium theory (EMT). The latter, establishes a relation between the compressional wave velocity anomalies, the mineralogy of the host sediment and the hydrate morphology and fraction *(Helgerud et al., 1999)*.

Many research studies used this method in order to quantify GH in marine sediments. For instance, *Carcione and Gei (2004)*, used the EMT in order to estimate concentrations of GH in the Mallik 2L-38 research well, Canada. Results derived from P and S wave velocities were found comparable to those obtained from Archie's method. Additionally, *Chand et al. (2004)* have showed that for clayey sediments at ODP sites 995 and 997, the EMT results are highly

59 comparable with those derived from electrical resistivity. Moreover, it was observed that for a
60 clay-hydrate system, it is more suitable to assume that hydrates affect the rock framework rather
61 than the pore fluid. Guerin et al. (1999) investigated GH occurrence in the Blake Ridge (ODP
62 Program Leg 164), where it was observed that hydrates increase the bulk modulus of the host
63 sediment. The rest of the results showed that GH estimates derived from assuming that hydrates
64 are acting as a cementing agent are very comparable to those derived from resistivity logs. Kim
65 et al. (2013) predicted GH contents using the EMT in the Ulleung Basin, which were later
66 compared to results from electrical resistivity and from an empirical Archie-analysis. Results have
67 shown that using EMT with a detailed mineralogy is a reliable method when estimating GH
68 contents. Wang et al. (2011) used the EMT and compared it to other quantification methods such
69 as chlorinity analysis and electrical resistivity within the clayey sediments of the Shenhu area,
70 South China Sea. Compared with other methods, results from the EMT were found rather
71 satisfactory.

72 The presence of GH in the marine environment dramatically alters the physical properties of the
73 host sediment by replacing the pore water /or gas with a solid compound. The compressional
74 wave velocity of GH-bearing sediments is much higher than that of sediments without hydrate.
75 On the contrary, free-gas bearing sediments tend to show negative compressional velocity
76 anomalies.
77 Those different approaches are often based on a well-known mineralogy of the host sediment
78 column (by coring or drilling) and on the difference between a reference sonic velocity profile
79 with respect to the one altered by the presence of free gas and GH. However, the use of in-situ
80 acoustic measurements to quantify GH as proposed by *Sultan et al. (2010)* is restricted by the
81 requirement to characterise the in-situ mineralogy of the host sediment.
82 Previously, *Taleb et al. (2018)* have discussed the effect of GH content and morphology on the
83 hydro mechanical properties of their host clayey sediments. In order to carry out this work, GH
84 quantification at certain measuring sites was conducted using the EMT. The aim of the present

paper is to expand on this previous work, especially by integrating the results of in-situ measurements with seismic data. This is achieved through a detailed review of the different steps followed in order to use the EMT, with special emphasis on the establishment of a petrophysical model and the derivation of mineralogical profiles from in-situ acoustic attenuation data. This was carried out by performing correlations between different laboratory and in-situ data before comparing the similarities and the differences between reference sites without GH and GH-bearing sites. This proved effective in detecting and quantifying GH based on in-situ acoustic measurements even for sediments where accurate mineralogical characterisation is not available.

Numerous oceanographic campaigns, aiming to study GH distribution, have been carried out along the Gulf of Guinea, which is known to accommodate dense accumulations of shallow GH *(Cunningham and Lindholm, 2000; Sultan et al., 2010; Wei et al., 2015)*. The study area is also characterised by the presence of different seabed deformations known as pockmarks. However, little has been discussed concerning the distribution of GH below the seabed and its impact on the shapes and sizes of these pockmarks. As a step towards identifying links between GH and free gas and the geometrical features of different pockmarks, the second aim of this paper is to correlate seismic data profiles and seabed morphologies with GH content. Analysing the geophysical signatures of GH accumulations and extrapolating all the available in-situ data using seismic profiles would indeed be helpful in the process of (1) characterising the sub-seafloor distribution of GH and (2) determining the relationship between hydrate distribution and seafloor depressions.

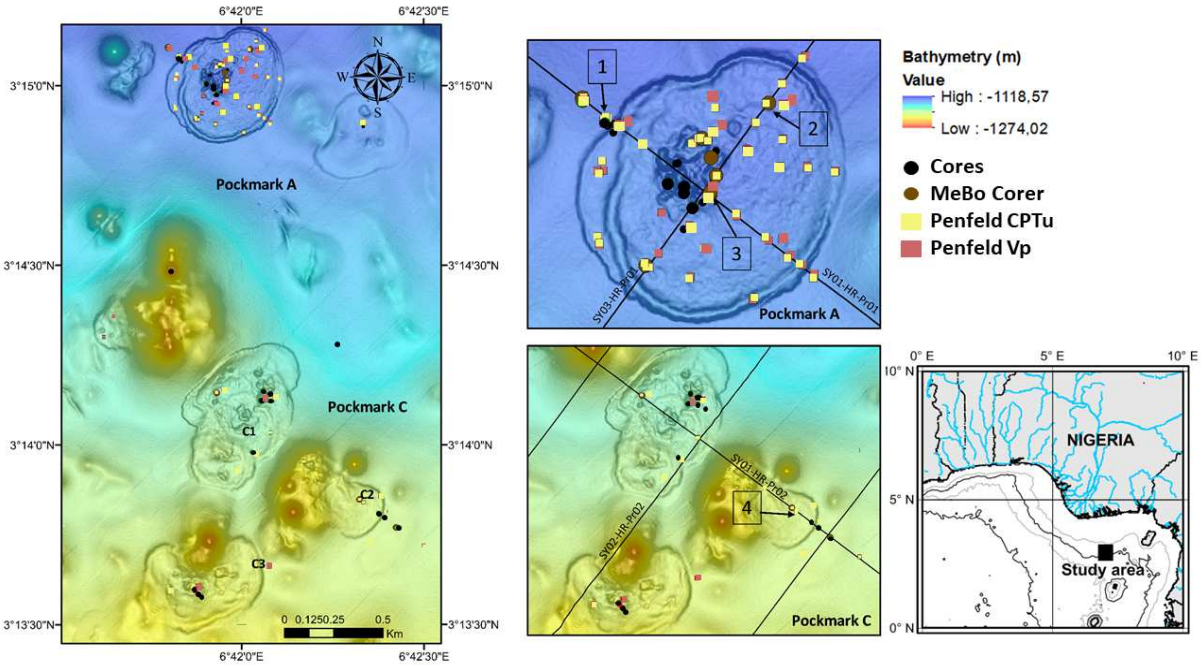
2. Study area

The study area is located in the Gulf of Guinea, in the southern part of Nigeria, off the Niger Delta. Numerous studies have shown that this area is characterised by various seabed features such as pockmarks which were directly linked to the formation and dissolution of GH

110 *(Sultan et al., 2014)*. The GH stability zone in the study area was found to expand from 90
111 mbsf to 120 mbsf as reported by *Sultan et al. (2010)*.
112 This paper focuses on two specific pockmarks that are referred to as A and C. Pockmark A is
113 situated in the northern part of the study area at depths lying between 1100 and 1200m
114 (Figure 1). It is 600 meters in diameter with a 6 meters deep peripheral depression.
115 Pockmark C is composed of a cluster of three sub-pockmarks revealing irregular seabed
116 morphologies: C1, C2 and C3 (Figure 1) located at water depths ranging from 1170 m and
117 1210 m. All four pockmarks are characterised by numerous moats and bumps on their
118 surface. While the area is classified as a high gas flux system fed by deeply sourced gas
119 through faults and fractures *(Sultan et al., 2016)*, GH have only been identified within
120 pockmarks.
121 *Wei et al. (2015)* have defined GH occurrence zones (GHOZ) based on pore water chloride
122 analyses and infrared thermal imaging. *Sultan et al. (2010)* have shown that the study area
123 accommodates shallow GH formation and identified zones where solid GH and free gas
124 coexist.

125 **3. Tools and methods**

126 Several cruises have been conducted in order to characterise the presence of GH in the study
127 area. The Guineco-MeBo (2011) and ERIG3D (2008) oceanographic campaigns took place on the
128 French R/V *'Pourquoi pas?'* and the NERIS2 (2004) on the R/V *'Atalante'*. All campaigns aimed to
129 determine the distribution of GH in the study area in order to understand the link between GH
130 and the mechanisms/formation and evolution of pockmarks as well as study the stability of
131 sedimentary bodies.



132

133 *Figure 1. Bathymetry of the study area showing seismic profiles through pockmarks and the investigated sites: 1:*
134 *GMPFV07S05, GMMB01 and GMCS05, 2: GMPFV03S03 and GMMB12, 3:GMPFV07S05, GMMB06 and ERCS02 and 4:*
135 *GMPFV10S04 and GMMB05*

Penfeld Vp site	Depth (m)	Length (m)	Nearby Calypso or MeBo cores	Site	Location
GMPFV07S01	1140	30	GMMB01 GMCS05	1	NE - Outside of pockmark A
GMPFV03S03	1142	101.3	GMMB12	2	NW pockmark A
GMPFV07S05	1146	8.5	GMMB06 ERCS02	3	Centre of pockmark A
GMPFV10S04	1195	26	GMMB05	4	Eastern part of pockmark C2

136 *Table 1. Investigated sites within the study area: site 1 cluster characterises reference sediment without GH nor free gas*

137 *while clusters 2, 3 and 4 represent sediment where the presence of GH was suspected or proved.*

3.1 In-situ measurements and coring

3.1.1 Piezocone (Penfeld)

The Penfeld seabed rig developed by Ifremer was used to carry out the in-situ measurements. Continuous measurements were ensured by the penetration of a rod down to 30m below seabed at a standard rate of 2cm/s with a thrust of 40 kN *(Sultan et al., 2010)*. The rod can push two types of probes into the sediment to carry out piezocone or acoustic soundings.

Pressure compensated sensors in the piezocone include two different load cells to measure the tip resistance (q_c) and the sleeve friction (f_s) along with a differential pore pressure (Δu_2) sensor located immediately behind the cone (u_2 position).

Acoustic measurements can alternatively be carried out using the ultrasonic fork also pushed into the sediment at the rate of 2cm/s. One branch of the fork contains a 1MHz compressional wave source while the second one, located 7cm apart, and contains the receiver. This eventually allows measuring the velocity of compressional waves (Vp) up to 2200 m/s together with the attenuation ratio between the emitted and received signal. In addition, the load applied to push the fork in the sediment is continuously measured during acoustic sounding.

In this paper four Penfeld Vp were investigated as shown in Figure 1 and in Table 1: site 1: GMPFV07S01 (outside pockmark A), site 2: GMPFV03S03 (NW sector of pockmark A), site 3: GMPFV07S05 (centre of pockmark A) and site 4: GMPFV10S04 (eastern part of pockmark C).

3.1.2 Coring and drilling

Cores were recovered using the Calypso piston coring system from Ifremer and the seafloor drill rig MeBo from Marum *(Freudenthal and Wefer, 2007; Freudenthal and Wefer, 2015)*.

In this paper four MeBo cores (site1: GMMB01, site2: GMMB05, site 3: GMMB06 and site 4: GMMB12) and two Calypso cores (site 1: GMCS05 and site 3: ERCS02) allowed the investigation of the study area (Figure 1 and Table 1). These sites were particularly chosen because they are the closest to the Vp sites presented above; and therefore, the most comparable ones.

3.2 Laboratory testing

3.2.1 Multi Sensor Core Logging (MSCL), Acoustic measurements, X-ray diffraction (XRD) and X-ray fluorescence (XRF)

The P-wave velocity, Gamma density and magnetic susceptibility were measured on board using the MSCL (Geotech). Measurements were done every centimetre for cores without hydrate and every 2 cm for cores containing hydrate. in this paper, the density profile from core GMCS05 (site 1 in Figure 1) was taken as a reference. Additionally, an acoustic fork, similar to that used in-situ with the Penfeld was used in order to determine the acoustic properties of the sediment in the laboratory.

The mineralogical composition of core GMCS05 was determined using the X-ray diffraction (XRD) technique every 10cm. Besides, the geochemical composition of the sediment was determined on the archive halves of each core at a sampling interval of 2cm using an Avaatech X-ray fluorescence (XRF) core scanner. This test can be performed at 10KV and 30KV, which allows the detection of different chemical elements.

Correlating results from both methods (XRF and XRD) allowed determining the mineralogical fractions every 2 cm of core GMCS05 (see chapter 4.1.1: Mineralogy derived from XRF and XRD tests)

The XRF logging results were also interpreted in combination with acoustic measurements to determine the clay, calcite and quartz content within the sediment (see chapter 4.1.2: Mineralogy derived from in-situ acoustic measurements)

3.3 Seismic Survey

The SYSIF (SYstème SIsmique Fond de mer) is a deep-towed seismic system designed by Ifremer for high (HR: 250 – 1000 Hz) to very high resolution (VHR: 650 – 2000 Hz) near-bottom marine seismic surveys *(Marsset et al., 2010)*. The penetration depth below the seabed is inversely proportional to the resolution quality and depends on the type of the penetrated sediment. Its altitude above the seabed is set at 100 m to reduce the Fresnel area where the pressure field is very irregular, which improves the lateral resolution with respect to the surface *(Ker et al., 2012)*.

In the study area, several perpendicular SYSIF profiles have been acquired through pockmark A and C, which were used to correlate the acoustic/geotechnical data and the geomorphology of the pockmarks. This allowed understanding the distribution of GH and free gas within the pockmarks.

Additionally, sub-bottom profiles were acquired every 4 meters using an Autonomous Underwater Vehicle (AUV) in pockmark A with an average penetration depth of around 70 meters. The AUV system produces pulses of 2-16 kHz, which are continuously narrowed in order to get a constant resolution with increasing depth. These pulses are then correlated with the recorded seismic data allowing enhancing the vertical resolution. The system is efficiently designed to minimize the survey time and maintain the same measuring speed *(George and Cauquil, 2007)*; thus, resulting in an evenly dispersed data. This eventually allowed creating a 3D seismic data cube of the pockmark bathymetry and the GHOZ occupying this pockmark.

3.4 GH quantification

3.4.1 From pore-water chloride analysis

During GH formation, chloride ions are excluded from the clathrate cage *(Ussler and Paull, 2001)*; thus, salinity increases in the surrounding pore water. Therefore, upon core recovery, the dissociation of GH releases fresh water, which induces as negative anomalies on the pore-water chloride profiles *(Wei et al., 2015)*. Pore water was extracted using Rhizon samplers on 12 MeBo cores and then chloride concentrations were determined using ion chromatography while assuming the absence of sulfate *(Wei et al., 2015)*.

Malinverno et al. (2008) presented a method to estimate GH content (S_h) from chloride anomalies:

$$S_h = \frac{\beta(C_{cb}-C_{cm})}{C_{cm}+\beta(C_{cb}-C_{cm})} \quad (1)$$

Where β is a coefficient that accounting for density change and equals 1.257, C_{cb} is the pore water chlorinity before GH dissociation measured in near-surface sediments and C_{cm} is the core chlorinity measured after GH dissociation.

Malinverno et al. (2008) described the C_{cb} parameter as critical to determine. Indeed the rapid in-situ formation of GH, which translates into positive chloride anomalies, can affect the baseline salinity prior to core recovery. The estimation of the baseline chlorinity at each GH-bearing site was not possible. The lack of such information poses limitations for this method. Therefore, in this work, the baseline chlorinity was defined based on a reference site where no gas hydrates nor free gas were detected as seen in *Wei et al. (2015)*. C_{cb} values were observed to oscillate around $550\ mM$.

3.4.2 From in-situ Vp measurements and rock physics characterisation

In this work, the EMT developed by *Helgerud et al. (1999)* has been used to estimate GH content in the sediment by relating the stiffness of the dry frame to porosity, mineralogy and effective stress. The model allows estimating a lower (S_{hmin}) and upper bound (S_{hmax}) of hydrate content, by alternatively assuming that a) hydrate alters only the pore fluid elastic properties (S_{hmax}); b) hydrate contributes stiffness to the sediment by becoming part of the load-bearing framework (S_{hmin}) *(Helgerud et al., 1999; Taleb et al., 2018)*.

Input parameters such as the porosity and the mineralogy profile were determined from sediment core GMCS05 (site 1 in Figure 1). Table 2 shows the elastic properties and density used in this paper *(Helgerud et al., 1999)*

Constituent m	$K(GPa)$	$G(GPa)$	$\rho(g/cm^3)$
Clay	20.9	6.85	2.58
Calcite	76.8	32	2.71
Quartz	36.6	45	2.65
GH	7.9	3.3	0.90
Water	2.4-2.6	0	1.032
Methane Gas	0.10-0.12	0	0.23

Table 2. Elastic and density properties of selected sediment components (after Helgerud et al. 1999). K is the bulk modulus, G the shear modulus and ρ the density.

4. Results

4.1 Mineralogical Analysis

In order to apply the EMT and quantify the concentration of hydrates in sediments, the mineralogy profile characterising the sediment in question must be defined.

The mineralogical composition of the reference sediment from site GMCS05 is presented in Figure 2, where it can be observed that the profile is dominated by clay and calcite with a low quartz fraction. While the clay fraction varies between 0.5 and 0.93, the calcite fraction varies between 0.01 and 0.42 and the quartz fraction is observed to have a quasi-constant value of around 0.06 with depth. Microscopic observations of the particle fraction larger than 63 µm reveal that fluctuations in calcite content are related to the foraminifera content and not to the presence of authigenic carbonates (Figure 2).

These XRD results were compared to those acquired with the XRF method in an attempt to obtain mineralogy profiles with a spacing of 2cm along cores.

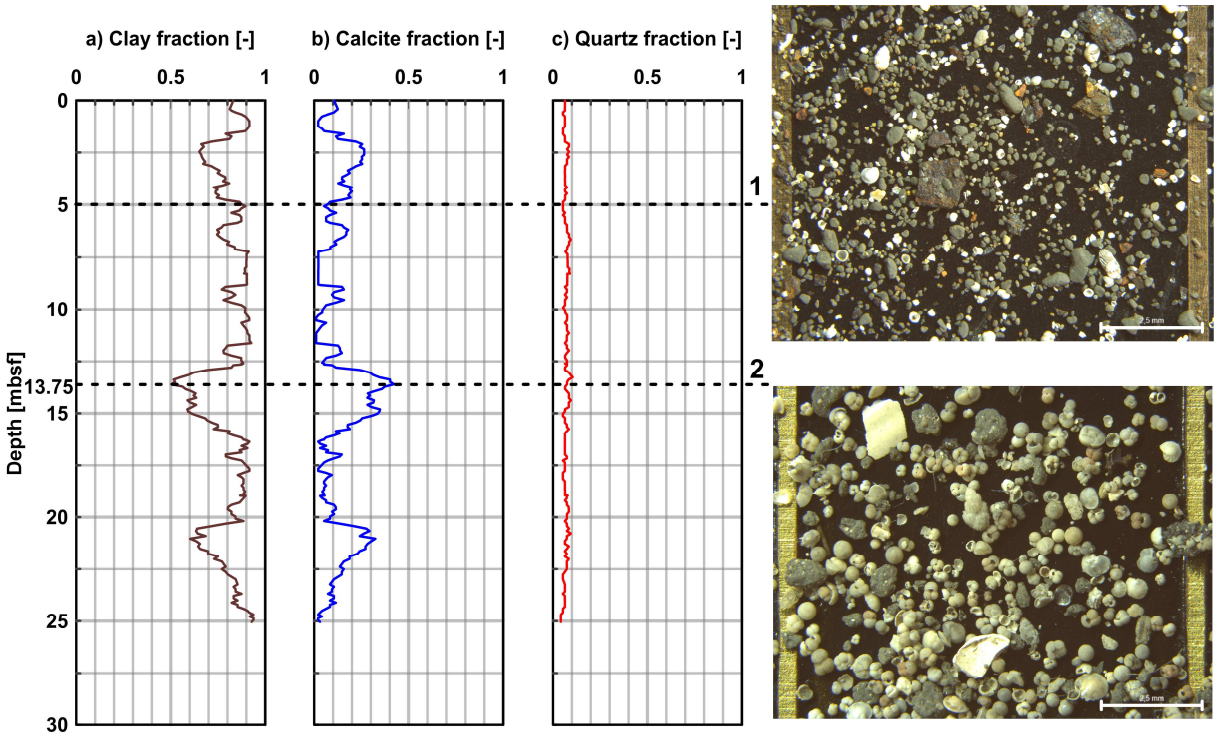


Figure 2. Mineralogy profile for reference site GMCS05 (site 1 in Figure 1): a) clay fraction, b) calcite fraction and c) quartz fraction. Pictures to the right show the particule fractions larger than 63 µm to be dominated by: 1) Rare benthic

foraminifera Uvigerina peregrina, Gyroidina sp. and 2) Abundant planktonic foraminifera Globigerinoides ruber, Globorotalia menardii, Neogloboquadrina dutertrei

4.1.1 Mineralogy derived from XRF and XRD tests

Correlations between XRD and XRF for reference core GMCS05 (site 1 in Figure 1) showed that the concentration of calcite ($CaCo_3$) can be linearly related to that of calcium oxide (CaO) (Figure 3). Therefore, the following equation was proposed to determine the proportions of calcite based on the calcium oxide content in cases where the former is not available:

$$CaCO_3\ (\%) = A \times CaO\ (\%) \quad (2)$$

Where A is the slope of the fitting line and is equal to 0.7 (red line in Figure 3)

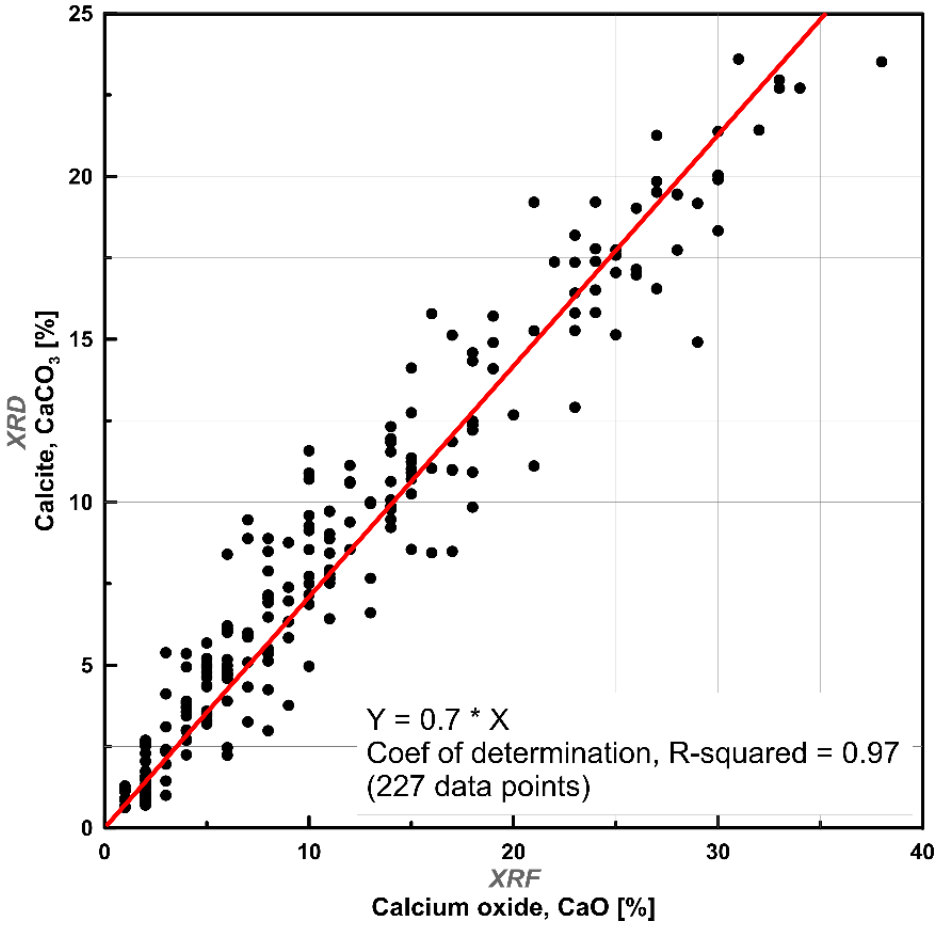


Figure 3. Correlation of calcite fraction with calcium oxide fraction for core GMCS05

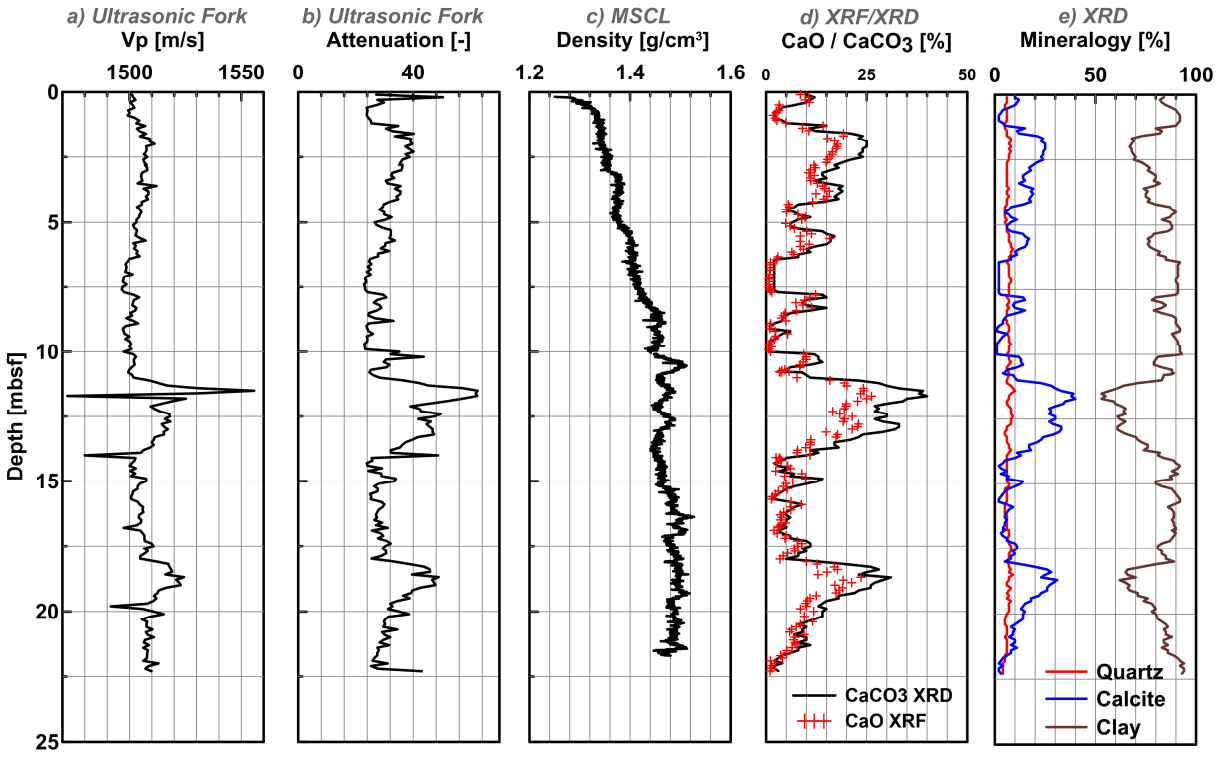
To further discuss the results at this stage, correlations between the mineralogical composition and acoustic data (Vp and attenuation) have been made (Figure 4).

Due to the high resemblance between the attenuation profile and calcium oxide/calcite content at reference site GMCS05 (site 1 in Figure 1), both profiles have been plotted against each other (Figure 5). With a regression coefficient R^2 of around 0.9, values of attenuation and calcium oxide/calcite follow a linear trend. This observation is important as it allowed determining calcite profiles at sites where XRF/XRD tests could have not been performed, mainly due to high disturbance of recovered cores in question, as shown in section 4.1.2.

However, in cases where the tested core was not disturbed, calcite profiles were determined either directly from XRD results or indirectly from XRF results using equation 2. For the quartz profile, values were considered constant and equal to the average quartz content (around 6%) in sediments from core GMCS05 (site 1 in Figure 1). The clay fraction is then calculated using the following equation:

$$f_{clay} = 1 - f_{calcite} - f_{quartz} \quad (3)$$

This allowed estimating the concentration of GH at all sites where Vp profiles were available.

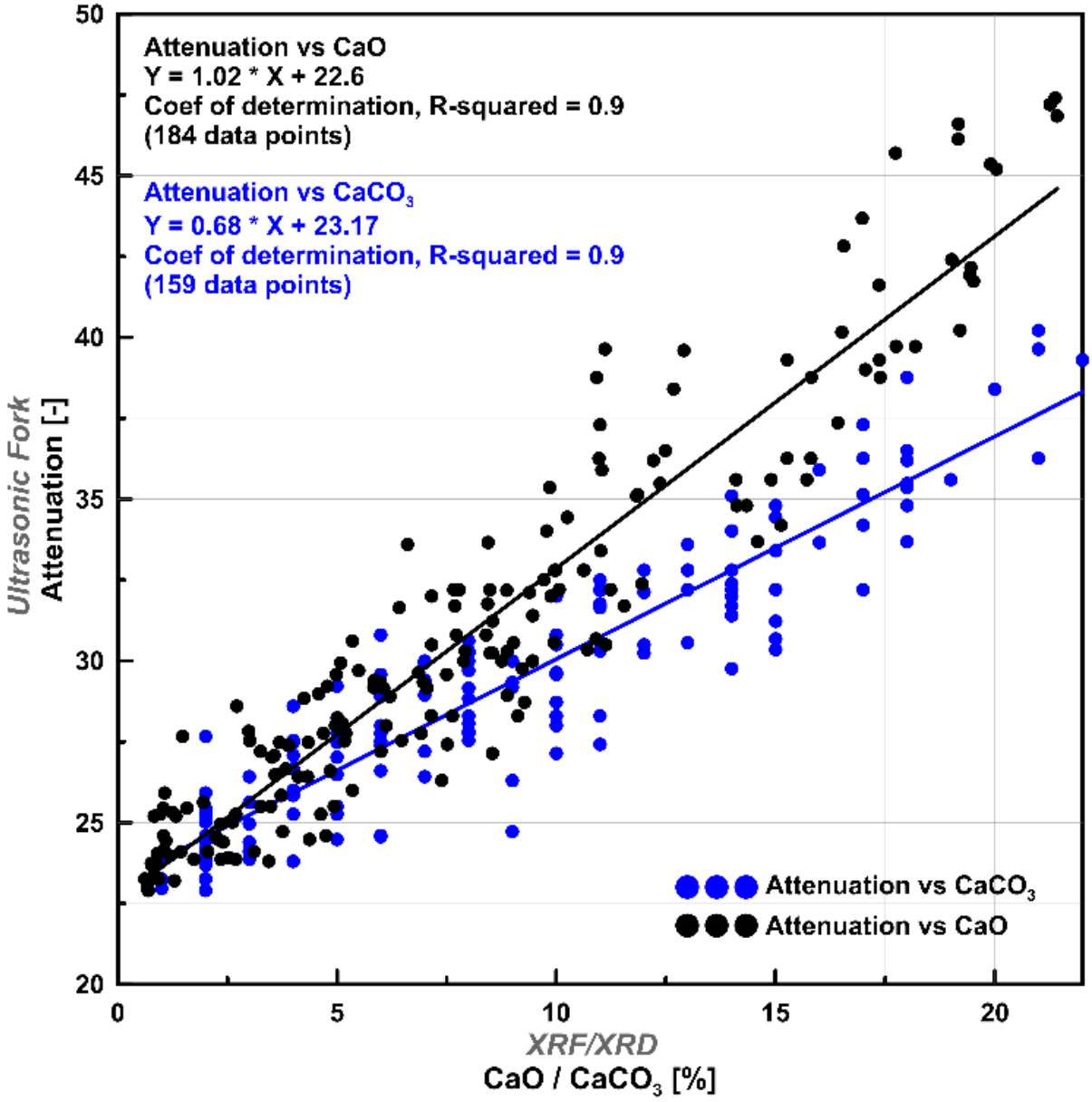


272

273 *Figure 4. Correlation between acoustic measurements for site GMCS05: a) compressional wave velocity and b) attenuation*

274 *and mineralogical composition: c) density, d) calcite (continuous black line) / calcium oxide (red crosses) and e) mineralogy*

275 *fractions (modified from Taleb et al. 2018).*

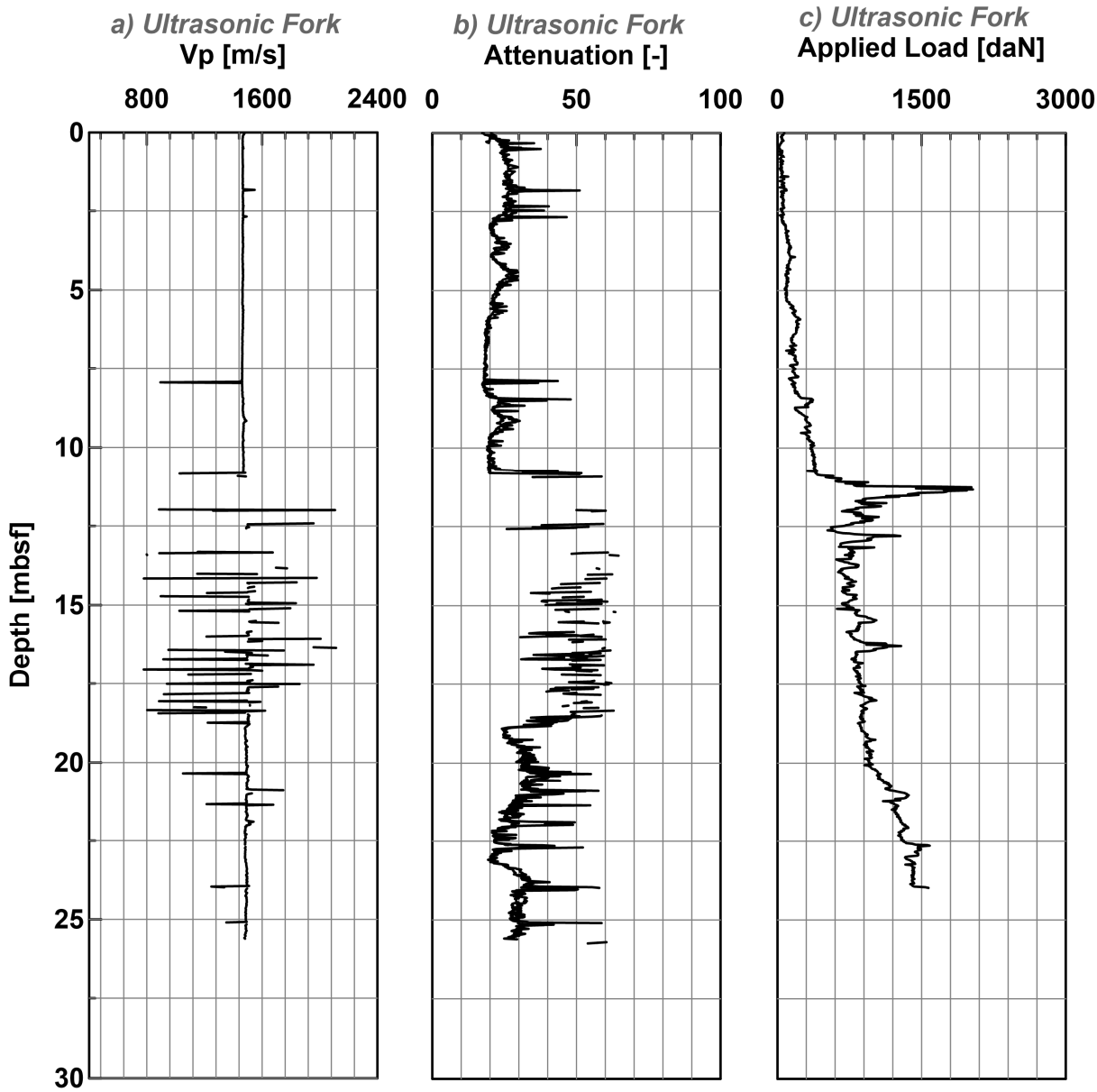


276

277 *Figure 5. Correlation of attenuation with calcium oxide and calcite fractions for core GMCS05*

278 4.1.2 Mineralogy derived from in-situ acoustic measurements

279 For some sites, XRF and XRD tests could not be carried out because of the absence of cores or the
280 disturbance of the sediment due to coring/drilling processes or GH dissociation upon core recovery.
281 The first step was to correlate all significant peaks and patterns of the in-situ compressional wave
282 velocity, the attenuation and the applied load profiles of the GH bearing site in question (Figure 6).



283

284 *Figure 6. GH bearing site GMPFV10S04 (site 4 in Figure 1) acquired by the ultrasonic fork: a) compressional wave velocity, b)*

285 *signal attenuation and c) applied load to penetrate the sediment.*

286 Based on earlier observations, the attenuation profile correlates best with that of calcite. Then, the

287 attenuation profile of the investigated site can be compared and correlated with that of a reference

288 site without GH, where XRF/XRD tests have been performed and the mineralogy profile determined.

289 To improve correlation between profiles, data have been first adimensionalised (Figure 7) using the

290 following equation:

291 $$x = \frac{\bar{x} - x}{\sigma_x} \quad (4)$$

Where, x is the value that will be made dimensionless (i.e. attenuation, mineralogy profile), $\bar{x}$ and σ_x are the mean and standard deviation values for x.

As represented in Figure 7.a and b (using red crosses), correlations were made by relating depths of similar patterns in the attenuation profile of the reference and GH bearing sites. Then the adjusted attenuation profile of the reference site (blue line in Figure 7.c) was superimposed on that of the investigated site (black line in Figure 7.c). Eventually, the calcite profile was depth-adjusted with that of the updated attenuation profile following the same process (Figure 7.d).

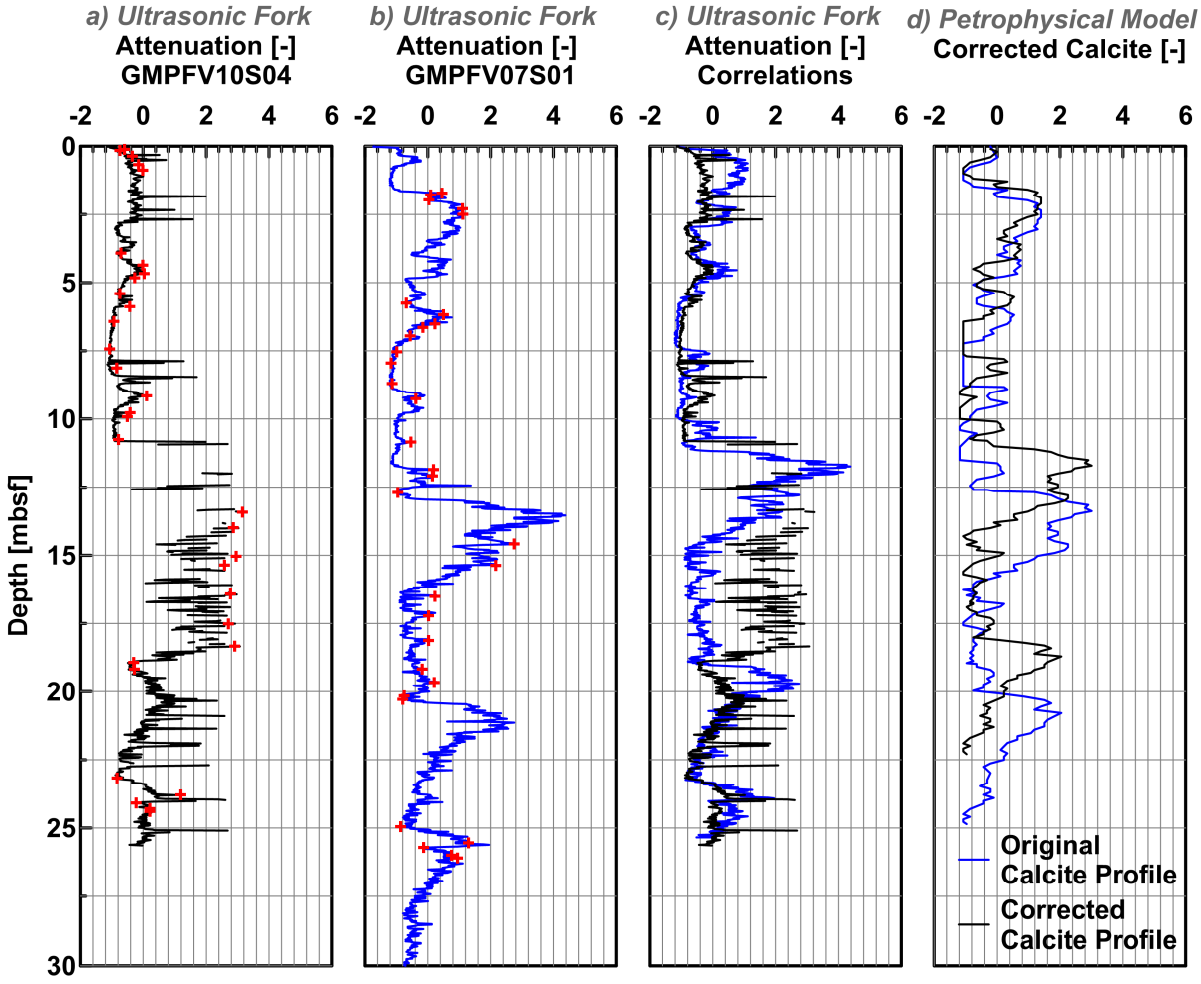


Figure 7. Correlations between adimensionalised attenuation profiles of: a) GH bearing site GMPFV10S04, b) attenuation profile of reference site GMPFV07S01, c) depth to depth correlation in terms of attenuation and d) adimensionalised original calcite profile (blue continuous line) against adimensionalised depth-adjusted calcite profile (black continuous line) that allow determining the mineralogy profile of GH bearing sediment at site GMPFV10S04 (blue curve in d).

For the quartz profile, values were set to a constant that is equal to the average quartz content in the sediment (around 6%).The clay fraction is then calculated using equation 3.

Examples of other depth-adjusted attenuation profiles are provided in **Appendix A**. The residual error resulting from assumptions concerning the quartz profile is shown in **Appendix B**.

4.2 Density Profile

The density profile is a substantial parameter in the process of the Vp inversion to estimate GH content (Figure 4.c). It allows calculating the vertical effective stress and porosity, which in turn are key parameters for the mathematical and physical equations used to calculate the content of GH in the sediment. The density profile of core GMCS05 (Figure 4.c) was used to define the reference compression index (C_c) and the initial void ratio (e_0) needed to determine the evolution of the void ratio (or porosity) with effective stress using the following equation:

$$e = e_0 - C_c . log \frac{\sigma'_v}{\sigma'_{v0}} \quad (5)$$

Where σ'_v is the vertical effective stress at a given level below the seabed and σ'_{v0} is a reference vertical effective stress taken equal to 1 kPa

From the density profile of GMCS05, values of 2.5 and 9.8 were estimated for C_c and e_0 respectively. They were considered as representative only for the first 30mbsf of sediment. These values were used to calculate the porosity and hence the bulk density for each site. The sediment bulk density (ρ_b) in this model is calculated as follows:

$$\rho_b = \phi\rho_w + (1-\phi)\rho_s \quad (6)$$

where, ρ_w is the water density

ρ_s is the solid phase density: $\rho_s = \sum_{i=1}^{m} f_i\rho_i$ (7)

f_i and ρ_i are the clay, calcite and quartz fractions and solid densities respectively.

The residual error resulting from the estimation of for C_c and e_0 is shown in **Appendix B**.

4.3 Back-calculation for GH content

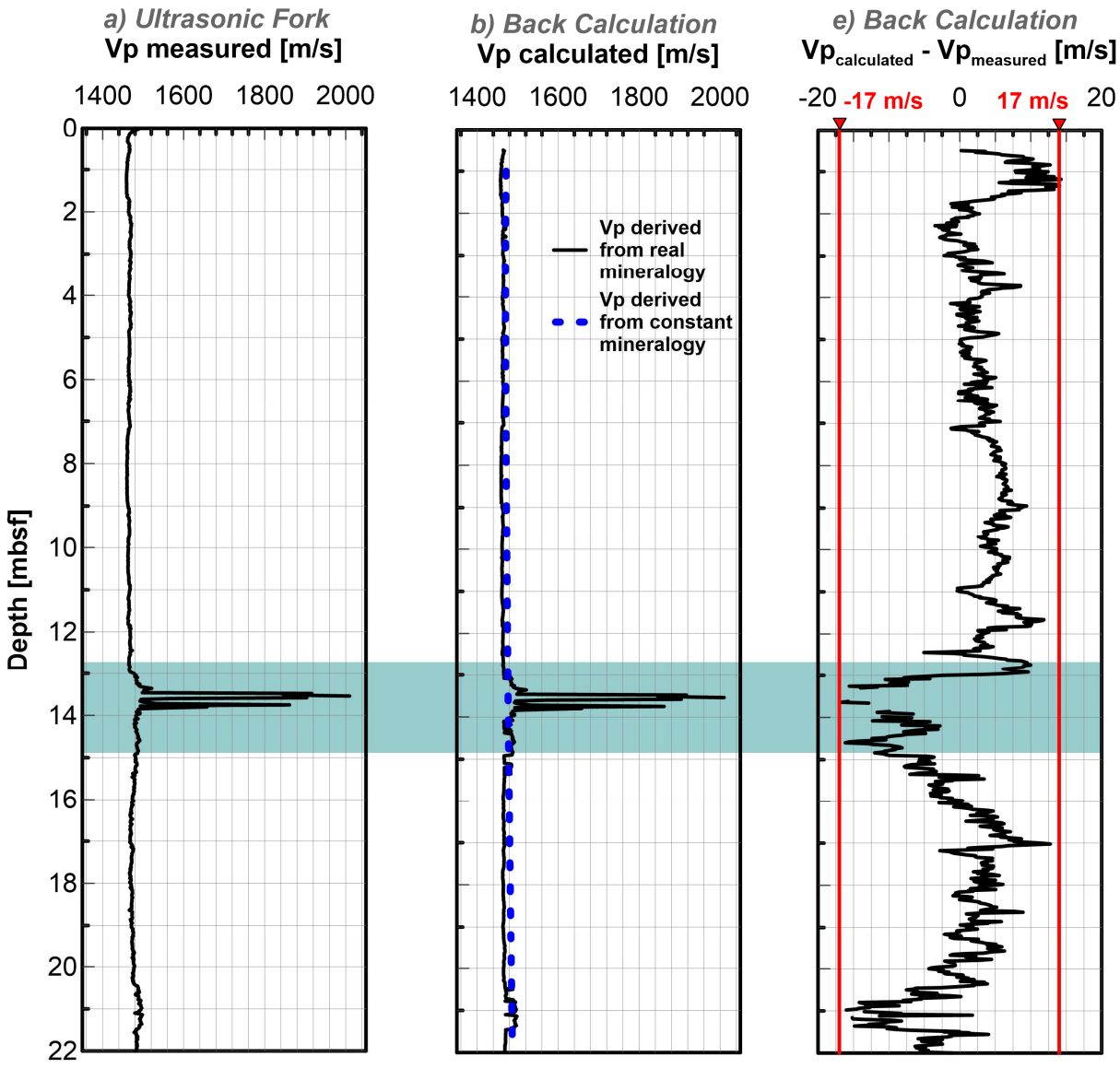
4.3.1 For reference site (no GH)

The GMPFV07S01 is a Penfeld Vp reference site at which neither GH nor free gas were detected. Based on Figure 8.a, reference sites are characterised by Vp oscillating between 1450 m/s and 1510 m/s; however, a clear peak of 2015 m/s is noticed at around 13.6 mbsf (blue rectangular zone in Figure 8). Such peak was related to the presence of foraminifera in the sediment *(Figure 2*).

Measured and calculated Vp are compared in Figure 8.a and Figure 8.b respectively. It can be observed that both profiles yield almost the same results, which proves the reliability of the EMT in reproducing the in-situ acoustic properties of the sediment.

Moreover, in order to highlight the importance of the mineralogy profile with respect to the quantification process, a mean mineralogy profile with constant fractions of clay, calcite and quartz is proposed. The new profile constitutes of 80.5% clay, 12.6% calcite and 6.9% quartz, which are the average values of each fraction respectively. The blue dashed line in Figure 8.b shows the calculated Vp profile derived from the new constant mineralogy profile, which oscillates around 1464 m/s and 1483 m/s. These values do not represent the real measured values from the Ultrasonic fork (black continuous line in Figure 2.b); hence, GH contents derived from such values will not be realistic nor representative of the sediment in question. Indeed mineralogical variations of the core are essential to capture its acoustic response, which is the main element in the quantification process of GH *Kim et al. (2013)*.

Additionally, to narrow down the calculation errors that could occur during the quantification process, the difference between the velocity calculated by the model and the measured velocity was calculated and found to oscillate in the range $\pm 17\ m/s$. Hence, GH contents will only be determined when the difference between the calculated and measured Vp is greater than $17 m/s$.



350

351 *Figure 8. Reference site GMPFV07S01 (site 1 in Figure 1): a) Vp measured using in-situ tool, b) Vp calculated using effective*
352 *medium theory based on real (continuous black line) and constant (dotted blue line) mineralogy and c) difference between*
353 *calculated velocity and measured velocity (Modified from Taleb et al. 2018).*

354 4.3.2 For sediment with GH

355 GH were quantified at all sites where Vp data were available and after definition of the mineralogy
356 profile of the sediment in question, which was mostly done by correlating acoustic data (attenuation
357 profile) of GH bearing sites with that of reference sites. This is because, in most cases, recovered
358 cores from GH bearing sites are highly disturbed due to GH dissociation during their recovery.

Quantification results obtained from the EMT were compared to pore-water chloride analysis and pictures of nearby recovered cores, which allowed carrying out a more reliable investigation of GH bearing sediments.

Figure 9 presents the Vp, the signal attenuation and the applied load at site GMPFV03S03 (site 2 in Figure 1). The positive and simultaneous increases of all three parameters confirms the presence of GH at this site. On the other hand, negative Vp anomalies indicate the presence of free gas within the sediment; thus, allowing determining layers where solid hydrate and free gas coexist.

At 7.5 mbsf, missing data in the Vp and signal attenuation profiles correlates with an increase of around 560 daN of the applied load, which suggests that GH were touched at this depth. This is followed by sudden increases of up to 2131 m/s in Vp and 60 in the signal attenuation at 7.8 mbsf. These results have been compared to infrared thermal scanning performed by *Wei et al. (2015)*. The temperature

measurements that can be performed by the IR camera range from $-40°C$ to $+120°C$ with an accuracy of $\pm 2°C$. The difference between the surface temperature and the background temperature has been calculated in order to analyse the recovered core *(Wei et al., 2015)*. Anomalies higher than $1°C$ are interpreted as voids in the recovered core, while anomalies lower than $-2°C$ were considered as indicative of the presence of GH. Nearby core GMMB12 (Wei et al., 2015) revealed temperatures as low as 16°C, which is due to the endothermic dissociation of GH. These colder temperatures, compared to reference sediments, indeed confirm the presence of GH. The recovery of these cores promote GH dissociation and therefore gas release and sediment expansion, which can lead to sediment expulsion from the core section. At this stage, it is important to mention that MeBo cores are composed of 1.50 m long sections. Therefore, the case of sediment expulsion and the depth accuracy of the hydrate recovered thanks to the MeBo is limited by the section length. It is then reasonable to consider this IR method as an extra and qualitative means to confirm the presence of GH.

The GH contents estimated with the EMT were averaged over depth intervals of 10 cm and then compared to those obtained from pore-water chloride analyses. Using Vp data, maximum GH contents were estimated to occur at 7.85 mbsf with values of 27% for S_{hmin}, 76% for S_{hmax} while a lower value of 11.5% was estimated by using the pore-water chloride data.

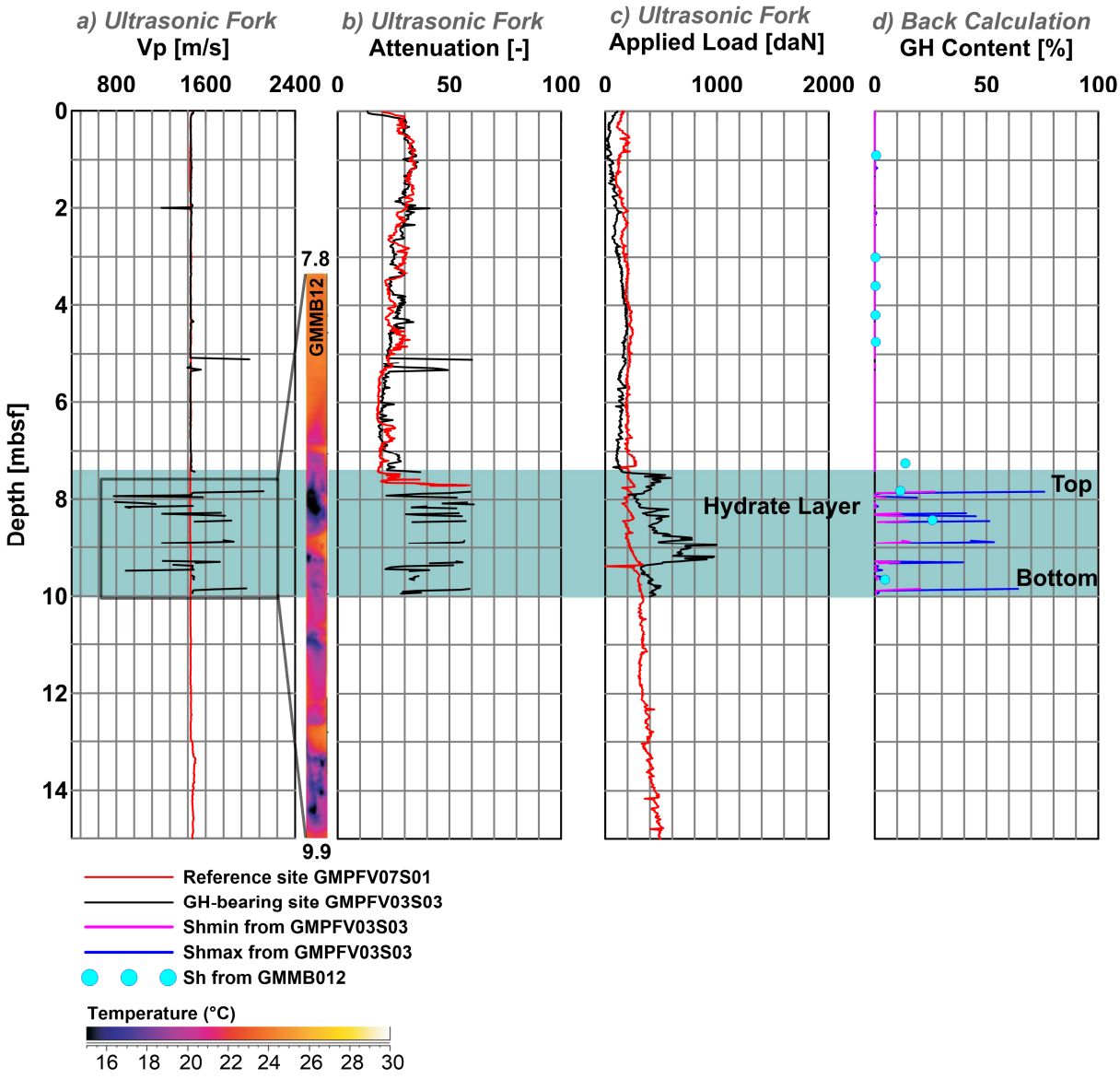


Figure 9. a) P-wave velocity, b) depth-adjusted attenuation profile, c) applied load for site GMPFV03S03 (black curves) against reference site GMPFV07S01 (blue curves) and d) GH content for site GMPFV03S03 (modified from Taleb et al. 2018).

For the GMPFV07S05 site shown in Figure 10 (site 3 in Figure 1) an abrupt increase in the applied load (1633 daN) at around 3.8 mbsf followed by a strong increase in Vp and signal attenuation (2050

m/s and 58 respectively) at 4 mbsf were observed. These values are up to 2 times higher than those obtained at the reference site at the same depths, which indicates the presence of GH. Additionally, photos of nearby Calypso core CS02 showed the presence of massive GH nodules followed by a 30 cm thick interval containing GH veins (Figure 10). Using the EMT, maximum GH content were estimated to occur at 4mbsf with values of 25% for S_{hmin} and 70% for S_{hmax}. At 4.3 mbsf, the GH content estimated from chloride concentration anomalies measured on MeBo core GMMB06 reaches 34%.

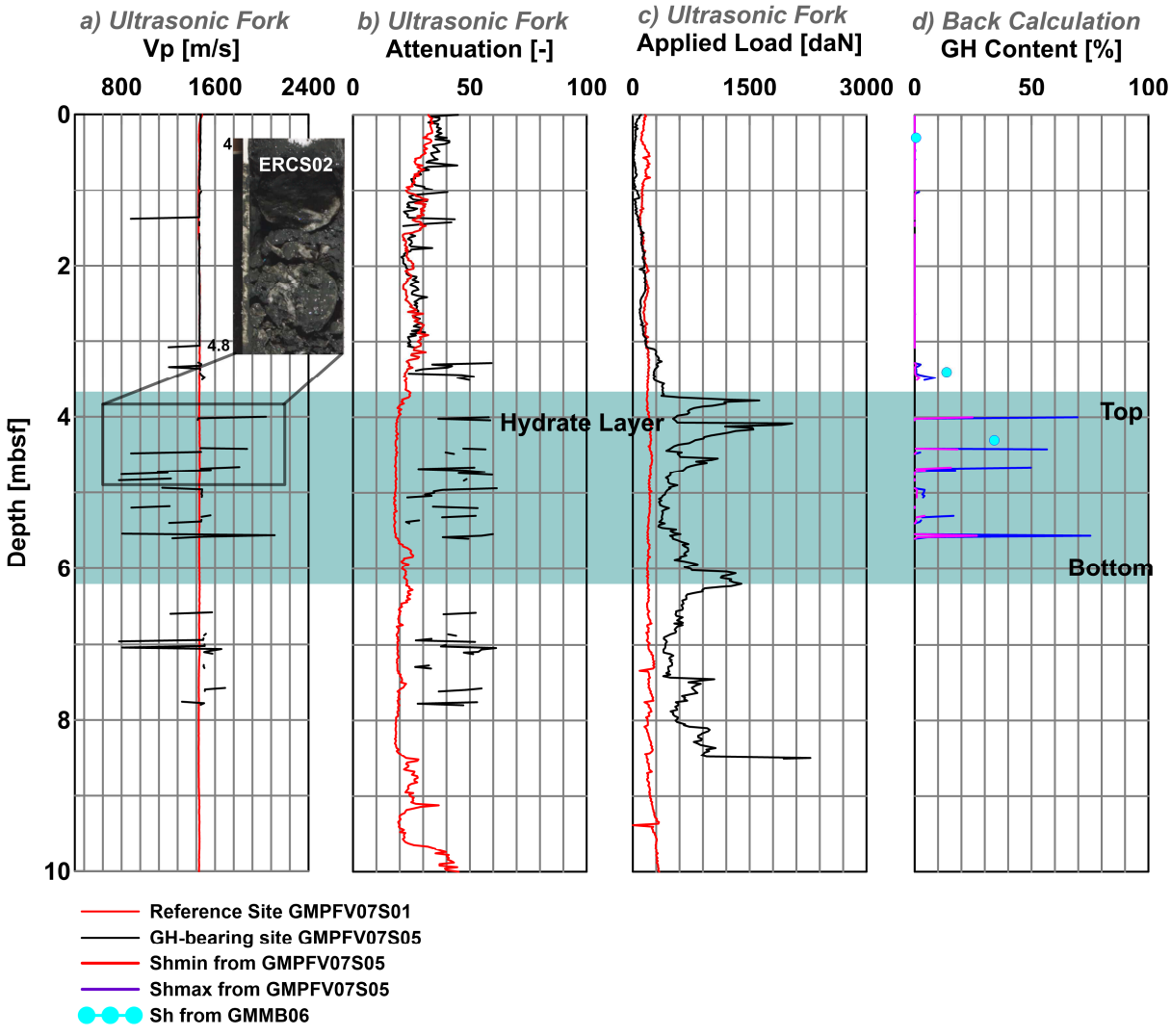
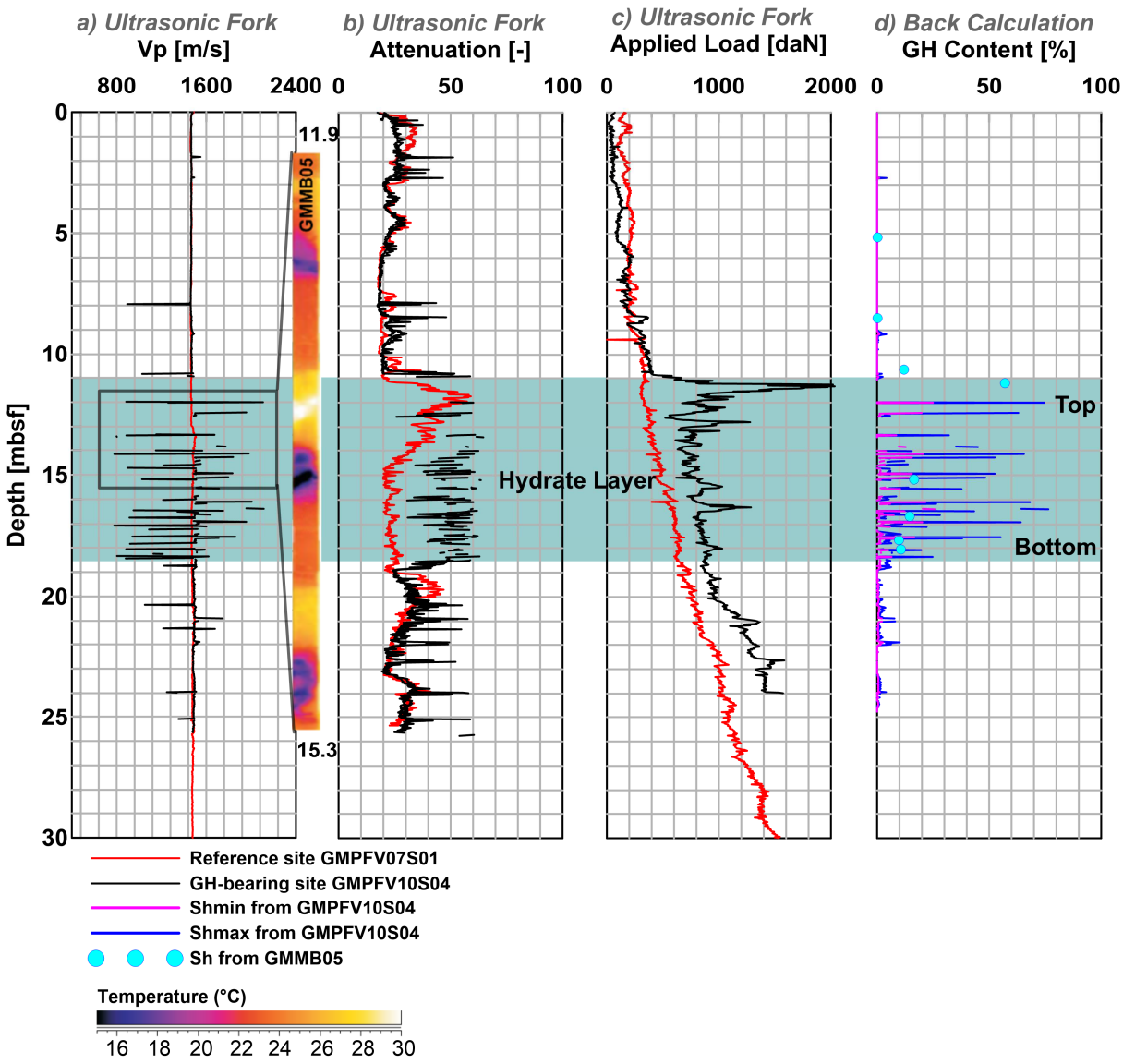


Figure 10. a) P-wave velocity, b) depth-adjusted attenuation profile, c) applied load for site GMPFV07S05 (black curves) against reference site GMPFV07S01 (blue curves) and d) GH content for site GMPFV07S05



403

404 *Figure 11. a) P-wave velocity, b) depth-adjusted attenuation profile, c) applied load for site GMPFV010S04 (black curves)*

405 *against reference site GMPFV07S01 (blue curves) and d) GH content for site GMPFV10S04*

406 Figure 11 presents the Vp, the signal attenuation and applied load profiles obtained at site

407 GMPFV10S04 together with estimates of GH content (site 4 in Figure 1). The presence of GH can be

408 confirmed due to simultaneous increases of in-situ acoustic parameters (Figure 11) and negative

409 thermal anomalies of the nearby core GMMB12 (Wei et al., 2015).

410 While missing data is observed in the P-wave velocity and attenuation profiles between 11 mbsf and

411 12 mbsf, the applied load profile suggests that GH were touched at 11 mbsf. This was confirmed by

412 the pore-water chloride data from which GH content as high as 57.5% was estimated to occur at 11.2

mbsf. This is followed by abrupt increases of 2111.2 m/s in Vp and 60 in signal attenuation, which highlights the effect of the presence of GH within the sediment. Maximum GH contents were found to occur at 12 mbsf with values of 20.5% for S_{hmin} and 75.6% for S_{hmax}.

Following previous work in *Taleb et al. (2018)*, GH contents derived from the EMT were compared with those derived from the pore-water chloride analysis. This showed that estimates of GH contents relying on the assumption that hydrate contributes to the stiffness of the sediment by becoming part of the load-bearing framework (S_{hmin}) are closer to those obtained from the chlorinity data. Hence, in the rest of this work only S_{hmin} (referred to S_h in the following) values will be considered and discussed.

4.4 Correlation between estimates GH content and seismic signatures

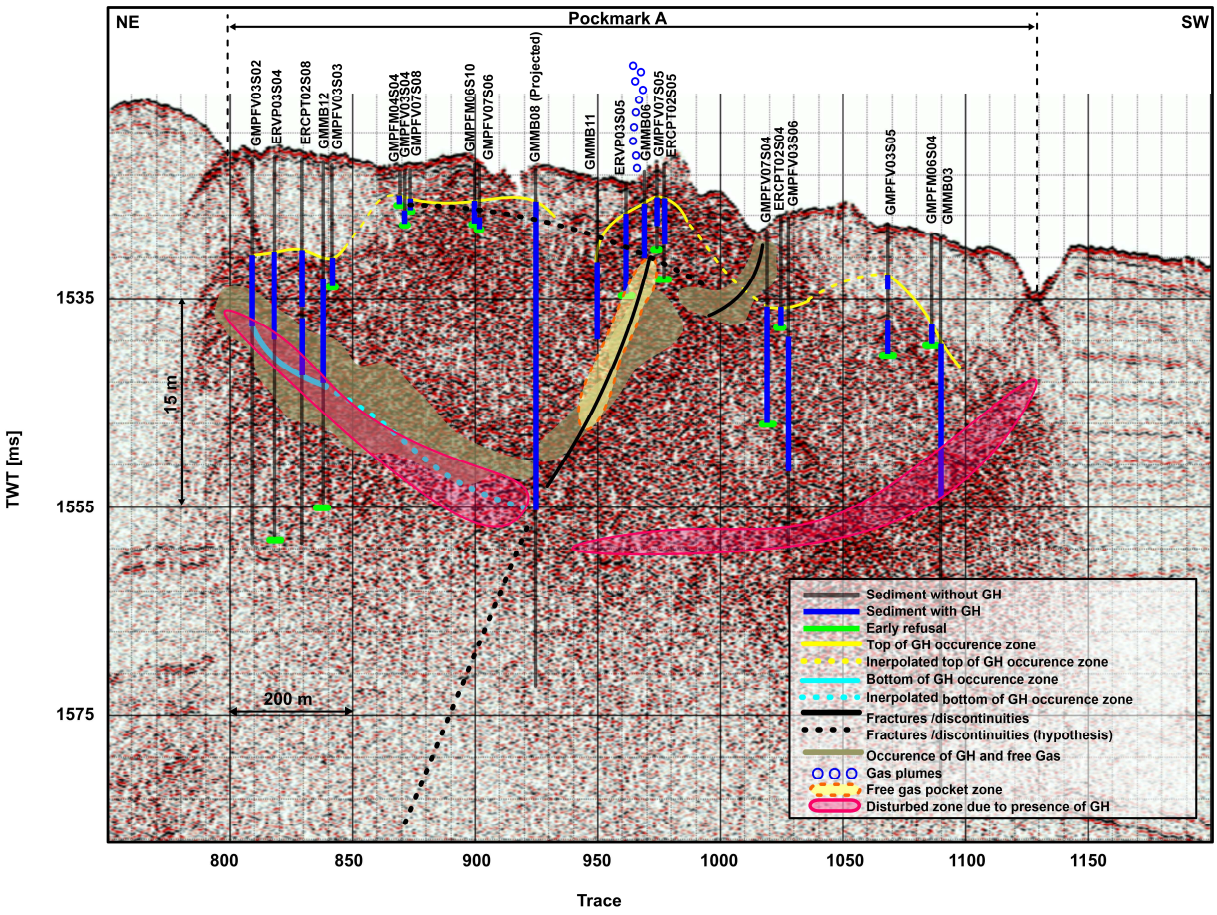


Figure 12. Seismic profile SY03-HR-Pr01 showing a marked contrast between the high-amplitude chaotic facies in the central part of pockmark A and the continuous sub-parallel facies of the surrounding sediments. Blue hollow circles indicate the flow path of free gas visually observed during drilling at site GMMB06.

As shown in Figure 1 and Figure 12, a number of in-situ measurements and cores can be tied to seismic profile SY03-HR-Pr01 in order to analyse the larger scale distribution and morpholgy of GH present within pockmark A and define the top and in some cases the bottom of the GHOZ.

In Figure 12 a significant contrast is observed between the high-amplitude chaotic facies in the central part of pockmark A and the continuous facies of low-amplitude sub parallel reflectors outside of its peripheral depression. In most zones, the top of the high-amplitude chaotic facies is observed to correlate with the top of GHOZ as infered from the analysis of in-situ and core data (yellow continuous line in Figure 12). Delineating the base of GHOZ proved much more difficult since at almost all sites early refusals were met during acoustic soundings (green segments in Figure 12). Early refusals suggest that the top of a second GH layer has been probably reached. The depths at which they occurred generally correlate with the presence of chaotic facies of higher energy on seismic profile SY03-HR-Pr01.These observations were found to almost correlate with the GH and free gas occurrence zones (light green zones on Figure 12) proposed by *Sultan et al. (2014)*.

On both sides of the profile, disturbed zones attributed to the presence of GH were highlighted (pink zones on Figure 12). They correspond to the top of a curved-shaped succession of hyperbolae interpreted as a zone of fractures/discontinuities suspected by *Sultan et al. (2014)*. In the central part of the NE-SW seismic profile (Figure 12), it is possible to identify the presence of fractures/discontinuities (solid black lines in Figure 12). These fractures are thought to be preferential paths for the free gas migration throughout the pockmark. This is further confirmed by this study based on visual observation of gas plumes at the centre of the pockmark (blue bubbles on Figure 12) and by the free gas pocket zone (light orange zone on Figure 12), which was discovered upon drilling at core GMMB11.

Alternatively, a total of 103 sub-bottom profiles in the x-axis direction and 124 in the y-axis direction were aquired from the C&C AUV survey within pockmark A *(George and Cauquil, 2007)*. In Figure 13.a, five sites (GMMB11, ERVP0305, GMMB06, GMPFV07S05 and ERCPT02S05) were projected on a seismic profile passing through the central part of pockmark A. It can be observed that the presence

of GH as infered from in-situ and laboratory measurements correlates well with the high-amplitude chaotic facies (dark zones in Figure 13), in a way such that the surrounding low amplitude to transparent facies (grey areas on Figure 13) is thought to be indicative of the absence of GH in sediments. All profiles were then analysed and used (Figure 13.b) to create a 3D seismic data cube and identify the GHOZ throughout pockmark A.

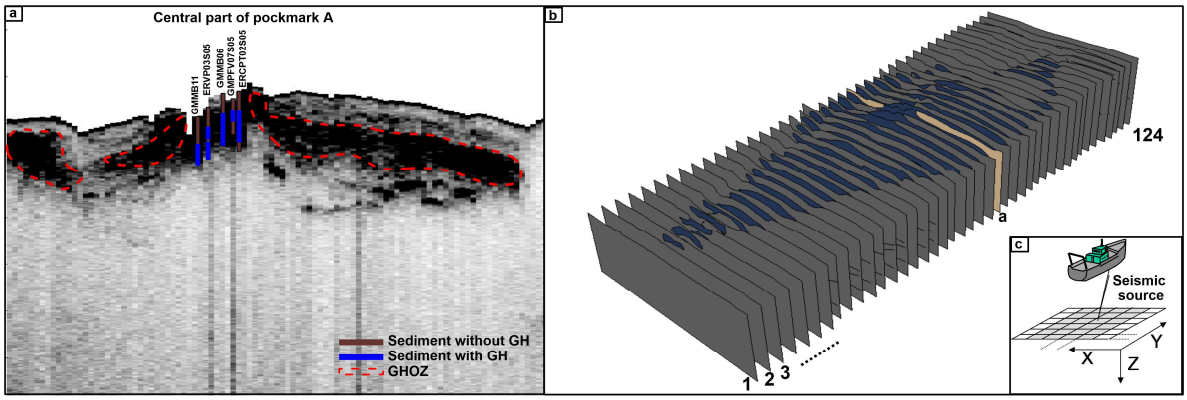


Figure 13. a) Seismic profile through the central part of pockmark A showing a sharp contrast between a high-amplitude chaotic facies (black zones) and a low-amplitude to transparent facies (grey areas), b) Seismic profiles in y-axis direction interpreted in order to create a 3D seismic data cube and c) illustration showing the directions in which the seismic profiles have been made.

5. Discussion

5.1 GH detection and quantification

In this paper, GH contents have been estimated from in-situ Vp measurements as well as from pore water chloride analyses carried out on adjacent cores. The presence of GH in clayey sediments was inferred from increases in P-wave velocity as well as from negative anomalies in the chlorinity and temperature profiles. Furthermore, positive anomalies in the attenuation and applied load profiles were also taken as an indicator of the presence of GH.

The quantification process required the use of a petrophysical model allowing sites lacking mineralogical input data to be correlated with reference sites, where background velocity

472 profiles and mineralogy are well defined. Using the EMT, a maximum GH content of 26.5% S_{hmin}
473 was estimated at a Vp of 2035 m/s.
474 It is arguable that relying on the assumption that GH contribute to the stiffness of their host
475 sediment is not suitable for the case of clayey sediments, which is characterised by the presence
476 of grain-displacing hydrates. Based on a comparative study conducted by Ghosh et al. (2010), the
477 method where GH are assumed to contribute to the stiffness of their host sediment (S_{hmin} in
478 this study) overestimates GH content by 7-11% with respect to the pressure coring method. Even
479 though the method proposed by *Ghosh et al. (2010)* to account for the grain-displacive
480 morphology is arguably the most accurate to quantify GH in clayey sediments, it could not be
481 used in this work due to a lack of quantification of the precise geometry and orientation of GH
482 within the sediment.
483 *(Shankar et al., 2013)* used the EMT to determine GH and free gas saturation in the Krishna-
484 Godavari Basin, eastern Indian margin. The basin is dominated by clayey sediments and it was
485 reported that GH occurred in fractures as veins or nodules. Numerical results have shown that
486 the effective medium models are more accurate compared with tested empirical models, since
487 the physical properties of the sediment were taken into consideration. Lee and Collett. (2009)
488 compared different GH estimation methods to the pressure core one while trying to account for
489 fracture orientation within the sediments. GH estimates derived from elastic velocities while
490 assuming high presence of angle fractures correlate well with the pressure coring method.
491 However, results have shown that the effect of fractures on GH content derived from electrical
492 resistivity and S-wave velocity is greater compared to values derived from P-wave velocity.
493 Furthermore, velocity-derived estimates of GH were compared to those derived from pore-water
494 chloride anomalies to evaluate the reliability of both upper and lower bound GH content.
495 Estimates assuming a load bearing contribution of hydrate to the mineral framework (S_{hmin})
496 were found to match better with the results derived from the chloride concentration anomalies

in pore water *(Taleb et al., 2018)*. Based on all these arguments, it was reasonable to consider S_{hmin} as the most representative of GH content in the study area.

On the other hand, one might argue that the pore-water chloride analysis can be associated with calculation uncertainties. Such method has been used in many research works *(Ussler and Paull, 2001; Torres et al. 2004; Riedel et al., 2005 and Riedel et al., 2006)*. Variables in equation 1 such as C_{cb} has been often considered as a limitation for this method. C_{cb} might be affected by the in-situ high pore fluid salinity caused by rapid GH formation or by in-situ low salinity caused by GH dissociation. At this stage, it is challenging to define an uncertainty range of C_{cb} in the case of the present work. However, *Riedel et al. (2006)* proposed a ± 0.5 (of standard deviation unit) range of uncertainty for C_{cb}. This range has been determined based on works performed by *Ussler and Paull (2001)* and *Torres et al. (2004)*. Moreover, *Joshi et al. (2018)* performed a study aiming at estimating GH saturation in the Krishna Godavari Basin. The authors derived GH content from measured and modelled velocities, which were later compared to GH content derived from pressure coring and chlorinity analysis. Results have shown that GH from chlorinity analysis as well as from pressure coring match well with those derived from the velocity inversion method.

Wang et al. (2011) compared results derived from EMT, while assuming GH as component of the solid phase, to those derived from chlorinity analysis. The depth intervals at which GH occurred were found similar in the case of both methods. Therefore, validating the comparative approach between different GH quantifying methods adopted in this paper.

Additionally, the distribution of GH within the study area has been discussed by Wei et al. (2015) based on negative thermal anomalies obtained from infrared imaging results. Looking at Figure 9 and Figure 11, it can be seen that the GHOZ determined by *Wei et al. (2015)* correlates well with that derived from EMT. This confirms that the presence of GH can be detected and quantified based on positive Vp anomalies.

Another limitation to the quantification of GH based on in-situ acoustic measurements is that the device used can detect compressional wave velocities only up to 2200 m/s. This has implications

especially where massive GH nodules were observed within the recovered cores between two layers of sediments. Based on laboratory analyses, one may indeed expect the Vp to increase to values higher than 3000 m/s in the presence of such massive GH nodules *(Helgerud et al., 2009)*. This could explain the discontinuities in the Vp profiles which precluded the exhaustive of GH.

One more constraint affecting the quantification of hydrates is the coexistence of free gas, which is known to decrease Vp (Helgerud et al., 1999). Because the effective medium model used solve equations with GH and free gas as two independent variables the actual GH content might have been locally underestimated.

5.2 3D model of pockmark A: seabed morphology versus hydrate/fluid distribution

Sultan et al. (2014) and *Wei et al. (2015)* have identified the different formation stages of the pockmarks within the study area, which is marked by a the presence of a graben bordered by deep seated faults through which gas migrates *(Marsset et al., 2018)*. The continuous supply of upward migrating gas has been considered as efficient enough to reopen sealed fractures or even create new ones. This would have promoted GH hydrate formation and consequent decreases in pore space and permeability. Such a situation is expected to have favored the development of overpressures and in turn that of new fractures/discontinuities.

Dewangan er al. (2010) investigated the seabed morphology and gas venting features in the region of Krishna-Godavari basin, where the presence of GH has been proved based on drilling and coring results *(Collett et al., 2008)*. According to *Bastia (2006)* the Krishna Godavari basin has similar geological features as those described by *Damuth (1994)* for the Nigerian continental margin. The area was observed to be characterised by several subsurface mounds, acoustic voids and acoustic chimneys, which were related to fluid/gas upward movements. This has led to the formation of muliple fractures and hence promoted accumulations of GH in the Krishna Godavari region similar to those found in the present study area *(Brooks et al., 2000)*.

Moreover, *Dewangan et al. (2010)* and *Riedel et al. (2010)* have discussed that the presence of faults in an area controls the distribution of GH accumulations, particularly the fracture filling type. *Gullapalli et al. (2019)*, investigated this fact by studying the implications of free gas migration on accumulations of GH using seismic data. Results have shown that free gas is migrating within the GH stability zone and promoting shallow GH accumulations. Such observations have been also previously reported by Wood et al. (2002) based on analysis of seismic data in the Cascadia margin, Canada.

In order to investigate the effect of the presence and distribution of GH on the geomorphology of the present pockmark, AUV seismic profiles through pockmark A *(George and Cauquil, 2007)* were used to illustrate the detailed architecture of GHOZ inside the pockmark. This eventually allowed calculating the GHOZ volume and its occupancy ratio in pockmark A (Figure 14).

In between the top and base of the GHOZ some intervals were delineated as zones where GH are absent. These so-called "GH free intervals" show three different shapes (A, B and C in Figure 14). By assuming that both GHOZ and the "GH free intervals" have an ellipsoidal shape, the total volume occupied by GH-bearing sediments was estimated to be on the order of $2.7 \times 10^6\ m^3$. Then, the GH volume was calculated by considering a mean hydrate fraction of 21%, which is the mean of all highest GH content at each site in pockmark A. This value is in accordance with results from Sultan et al. (2007) where GH content from 3D seismic data was found to be equal to 20% in pockmark A. Therefore, the GH volume was found equal to $0.57 \times 10^6\ m^3$. The total volume of the pockmark was estimated in order to determine the total occupancy of GH. Based on seismic data, pockmark A was assumed to extend down to 45 m below seafloor. Accordingly, GHOZ was found to occupy 17% of the total pockmark volume with a GH volume equivalent to $0.57 \times 10^6\ m^3$. It is debatable that such calculations might be outdated due to rapid formation and dissociation of GH in the study area. However, such mechanisms are localised in the shallow central part of the pockmark, which is only a small volume compared to the whole

pockmark. *Bayon et al. (2015)* carried out Uranium-Thorium dating on a carbonate-rich layer of a sediment recovered from the study area. Results have shown that carbonate precipitation related to intense fluid seepage has occurred between 13 and 10 ka. This proves that the present hydrate-pockmark is evolving since thousands of years.

Furthermore, two sections (NE-NW and SW-SE) were extracted from the 3D bathymetry (Figure 15). On both sections, seismic profiles were projected as well as GH contents from in-situ data and the GHOZ (blue zones in Figure 15) as outlined in Figure 14. These correlations indeed highlight the heterogeneous distribution of solid hydrate and free gas within the pockmark, which is an observation already reported by many authors in different GH-rich region *(see for instance Wang et al., 2011)*. Finally based on all these observations and analyses, a detailed description of the actual fluid/hydrate dynamic distribution within the pockmark can be proposed. The highest GH contents (20%-30%) are observed to be in the centre while lower contents (0%-10%) are mostly observed at the borders of the pockmark. This is in line with the actual morphology of the pockmark showing mostly bumps in the central part due to high content of GH and a slight depression on the borders where according to *Sultan et al. (2010)* GH might have dissolved. At this stage, it is intersting to note core GMMB08 (site11 in Figure 15.a) has been projected from a distance of 86 m, which explains why it intersects GH free intervals .

It is also noteworthy that the GH and free gas occurrence zones cover all the proposed fractures/discontinuities and disturbed zones shown in pink in Figure 12. *Taleb et al. (2018)* discussed the presence of GH having a spongy texture in the study area (light green zones in Figure 15) due to free gas being trapped within the pores of GH itself. This is due to the high gas flux present in the study area, which stimulates rapid GH formation; hence, causing the coexistence of both phases. In other cases, GH forms on the inner walls of the fractures/discontinuities, which isolate free gas from the surrounding pore water (yellow zone in Figure 15.a).

A bump can be observed at sites ERCPT02S05, GMPFV07S05 and GMMB06 (site 25, 26 and 27 in Figure 15.b). This is interesting since this location accomodates shallow GH with different morphologies *(Taleb et al. 2018)* such as massive nodules or thin veins (direct visual observations of core ERCS02 in Figure 10) as well as gas plumes at site GMMB06 (blue bubbles on Figure 12). Free gas might be escaping through fractures within the sediment and contributing to further shallow GH formation. These fracture zones have preferentially near-vertical orientations and contribute to the continuous supply of free gas, which in turn contributes to maintaining the presence of GH. Therefore, the bulge at this location might be formed to accommodate new GH formations and already existing high GH content. In other words, the shallowest GH accumulations in the pockmark are directly related to a central fracture or set of fractures that is supplying gas up to the water column. Lateral gas migration away from the central fracture, circulating from the highest to the lowest free gas/GH contents, is thought of as the most likely factor to explain why the shallow hydrate accumulation in the central part appears to follow the same geological horizons (Figure 13). All the processes here proposed would be directly or indirectly related to the vigorous gas flux through the central part of the pockmark as confirmed by the gas plumes in the water column and the free gas pocket zone (yellow line in Figure 15).

Thinner and deeper GH accumulations are generally observed in the peripheral depression of the pockmark (Figure 12 and sites 17 and 18 in Figure 15.a). This can be explained by the fact that GH in this part of the pockmark have already disappeared probably due to a dissolution process as described by *Sultan et al. (2014)* and to initially lower GH contents there as observed in Figure 15. Such phenomena is not considered to be caused by dissociation because at this depth stability conditions (low temperature and high pressure) for GH formation are respected.

These observations are in line with seismic characteristics discussed by *Kumar et al. (2019)* in order to detect the presence of solid GH and free gas. According to *Chand and Minshull (2003),* many seismic features can highlight the presence of GH and/or free gas, such as blanking and

622 vertical acoustic wipeouts. The latter has been reported by *Bouriak et al. (2000)* in the Storegga
623 slide area and has been related to upward fluid migration. Judd and Hovland (2009) indicated
624 that the escape of fluids to the seafloor is an important factor in pockmark formation that can be
625 mapped using seismic and bathymetry data. Furthermore, this migration does not only consist of
626 gas moving upward but also of heat, which can contribute to localised GH dissociation *(Chand*
627 *and Minshull, 2003).*

628 At this stage, a comparison between pockmark A and other pockmarks, highlighting the
629 similarities and differences, is interesting in order to further understand the geological features
630 of the study area. *Hovland and Svensen, (2006)* and *Vaular et al. (2010)* have performed studies
631 on the Nyegga pockmark in the mid-Norwegian margin, where the presence of GH has been
632 confirmed. The authors have proposed several stages that can promote GH formation: high gas
633 flux up to the seafloor and thermobaric conditions corresponding to the stability conditions of
634 GH. Similarly to pockmark A, the gas flux through the seafloor of the Nyegga pockmark is
635 heterogeneously distributed and GH forms where the flux is highest and in contact with water.
636 After comparing pockmarks A and C with that of the Nyegga region, it can be observed that they
637 share comparable dynamics: the morphology of the pockmark grows and collapses over time due
638 to cycles of formation and dissociation/dissolution of GH in the shallow sub-surface sediment. On
639 the other hand, *Sahling et al. (2008)* have studied three morphologically complex pockmarks (the
640 Kouilou pockmarks) in the northern Congo Fan area, where they proved the presence of a 25-30
641 m thick shallow GH layer. By contrast with that of the study area, pockmarks in Kouilou did not
642 exhibit gas venting features. This suggests that pockmarks in the study area are probably more
643 active with respect to free gas flux, compared to the Kouilou pockmarks; or that the last one is
644 probably in an earlier phase of GH formation. Additionally, *Riboulot et al. (2016)* have correlated
645 geophysical, sedimentological and geotechnical data in order to obtain insight into the inner
646 architecture of pockmarks situated in the eastern Niger submarine delta. The study showed that
647 the pathway through which the free gas is migrating and feeding the GHOZ is located beneath

the central part of the studied pockmark. This is in line with this work, since the highest GH contents were identified in the central part of pockmark A (at sites 14, 15 and 16 in Figure 15.a and sites 25, 26 and 27 in Figure 15.b). Furthermore, the GHOZ (Figure 14) has a similar geometry as the 3D bathymetry of pockmark A showing the influence of GH presence on the formation of the pockmark. All these findings confirm that GH content and distribution play an important role in shaping and forming of some pockmarks.

Therefore, complex seafloor morphologies, such as pockmarks, can be an indicator of the presence of GH *(Riboulot et al., 2016)* and must be considered as a potential source of geohazard particularly for industrial seabed developments (i.e. offshore operations, pipeline installations and well drilling). The correlations between in-situ acoustic and geotechnical measurements with the seismic data have indeed allowed understanding the link between the morphology of pockmark A and that of GH. This approach can be applied to other similar pockmarks, such as the Barents Sea pockmarks *(Chand et al., 2009)* or in the Norwegian Sea *(Hovland and Svensen, 2006)*, in order to define the sub-seabed distribution of GH as well as different formation stages of the geological features of the study area.

For future works, it would be interesting to compare the different shapes of the GHOZ seen in Figure 14 to the lithology of the surrounding sediment to highlight how porosity and permeability contrasts might have contributed to spatial distribution of GH.

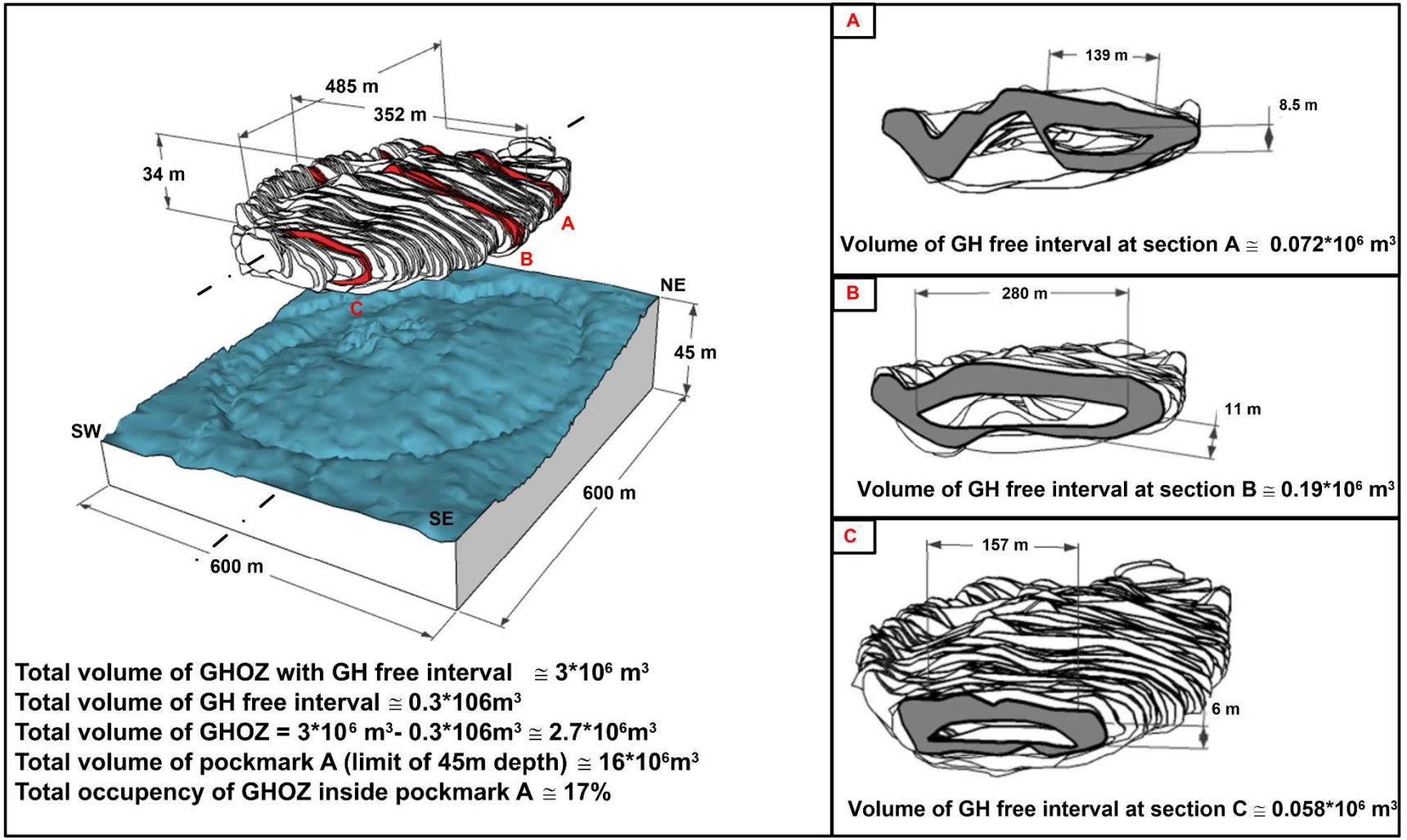


Figure 14. Left: 3D bathymetry of pockmark A compared with the GHOZ as mapped from seismic data. Right: illustration of the three distinct morphologies (A, B and C) of the GHOZ as mapped from seismic data.

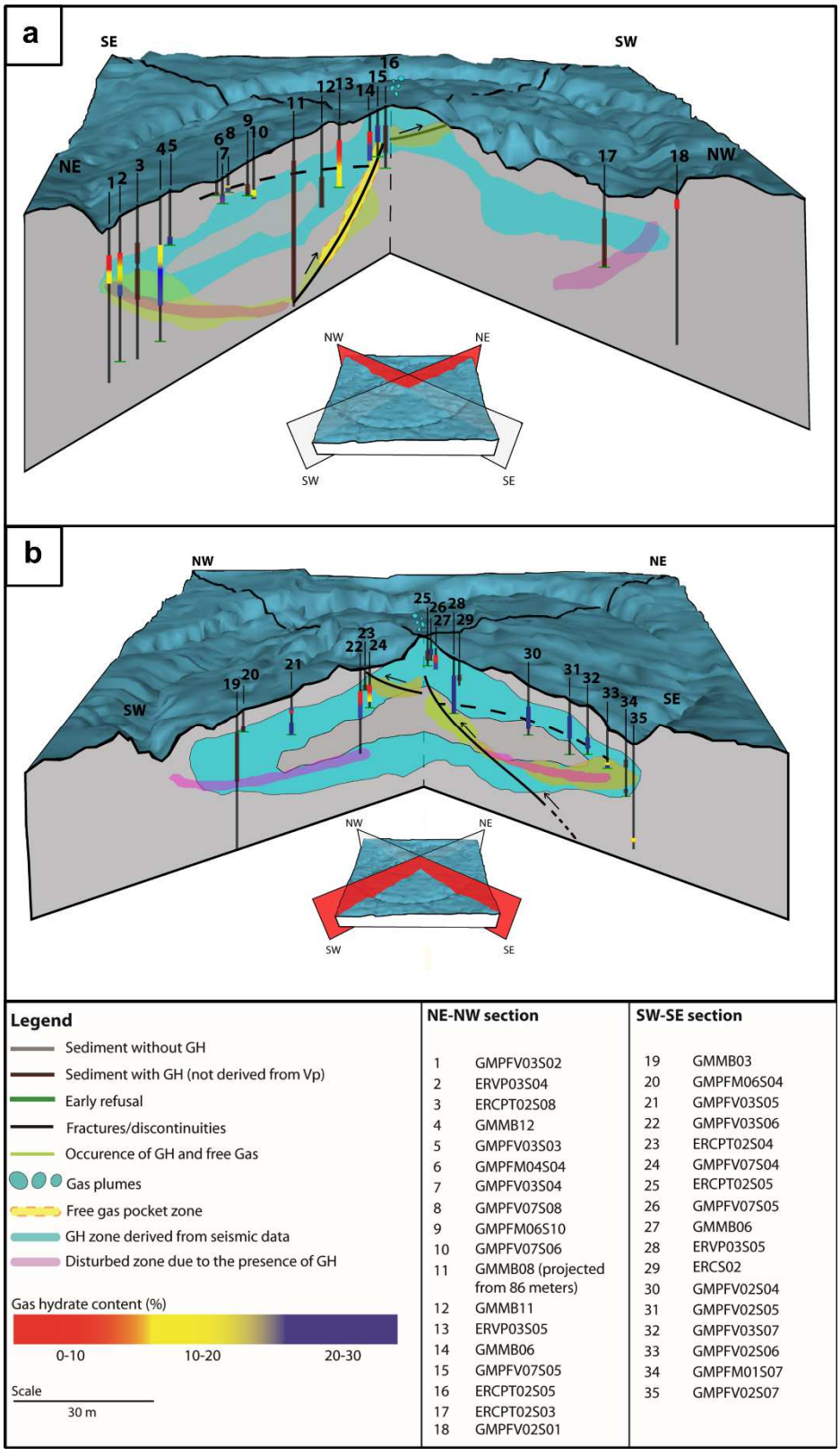


Figure 15. a) Perpendicular cross section across the northern part of pockmark A and b) perpendicular cross section across the southern part of pockmark. On each cross section GH contents as estimated from in-situ measurements as well as the GHOZ and fractures/discontinuities as inferred from seismic data are projected.

6. Conclusion

This paper aims to study the effect of GH content, distribution and morphology on the geomorphology and the actual state of the pockmarks present in the study area. This work mainly focused on pockmarks A and C in the Gulf of Guinea, where in-situ acoustic, coring and drilling data as well as seismic sections were acquired from different oceanographic campaigns. GH contents in the marine sediment were estimated using the Effective Medium Theory (EMT), which requires an accurate definition of the mineralogy profile. In cases, where the recovered cores were undisturbed, the mineral proportions were defined using the XRD and XRF techniques. In cases where the recovered cores were significantly disturbed due to GH dissociation, a petrophysical model based on the acoustic data of the site in question was developed and allowed determining the mineral proportions. The correlations and analysis of this unique database has led to the following conclusions:

1. Positive Vp anomalies along with simultaneous increase of the attenuation and applied load profiles are an indicator of the presence of GH.
2. A maximum GH content of 26.5% was estimated for a Vp of 2035 m/s using the EMT.
3. Results derived from the EMT and those from negative thermal and chloride anomalies were found to yield almost the same GHOZ
4. Correlations between seismic profiles and in-situ data as well as visual observations of recovered cores have shown that:
    a. High amplitude chaotic facies are an indicator of the presence of GH. However, low-amplitude subparallel facies represent undisturbed sediments.
    b. The study area accommodates zones where solid GH and free gas coexist as well as zones of free gas pockets.
    c. Fractures/discontinuities have been identified as preferential pathways in which free gas can migrate and contribute to further GH formations.

5. Extrapolation of in-situ and core measurements using seismic data indicate that with a volume of $2.7 \times 10^6\ m^3$the GHOZ occupies 17% of the total volume of pockmark A for an estimated GH volume of $0.57 \times 10^6\ m^3$.
6. The seabed morphology of pockmark A is directly influenced by the distribution of underlying GH accumulations:
    a. The highest GH contents (20%-30%) are observed to be in the central part of the pockmark, which is characterised by several bumps.
    b. The lowest GH contents (0%-10%) are mostly observed at the borders of the pockmarkwhich are characterised by a slight depression.
7. The morphology of a given pockmark in the study area might be an indication that can be used to confirm the presence of GH, determine an interval of GH content and identify different GH morphologies.

Acknowledgments

Data used in the present paper are covered by a confidentiality agreement between Total, Ifremer, and Marum that restrict access; interested readers can contact the authors for more information**.** We The authors would like to thank Natalia Vazquez Riveiros for help in providing the photos of the forams.

The authors would like to express their great appreciation to the *French National Research Agency* for funding the present study, which is part of the project *HYDRE "Mechanical behaviour of gas-hydrate-bearing sediments" – ANR-15-CE06-0008.*

719 **References**

720 Bayon, G., M, H.G., Joel, E., Jean-claude, C., Livio, R., Tania, M., Bernard, D., Eric, C., Michel, V., Nabil,
721 S., 2015. Achimer U-Th isotope constraints on gas hydrate and pockmark dynamics at the Niger
722 delta margin 370, 87–98.

723 Bastia, R. (2006). An overview of Indian sedimentary basins with special focus on emerging east coast
724 deepwater frontiers. The Leading Edge, 25(7), 818-829.

725 Bouriak, S., Vanneste, M., & Saoutkine, A. (2000). Inferred gas hydrates and clay diapirs near the
726 Storegga Slide on the southern edge of the Vøring Plateau, offshore Norway. Marine Geology,
727 163(1-4), 125-148.

728 Brooks, J. M., Bryant, W. R., Bernard, B. B., & Cameron, N. R. (2000). The nature of gas hydrates on
729 the Nigerian continental slope. ANNALS-NEW YORK ACADEMY OF SCIENCES, 912, 76-93.

730 Carcione, J. M., & Gei, D. (2004). Gas-hydrate concentration estimated from P-and S-wave velocities
731 at the Mallik 2L-38 research well, Mackenzie Delta, Canada. Journal of Applied Geophysics,
732 56(1), 73-78.

733 Chand, S., & Minshull, T. A. (2003). Seismic constraints on the effects of gas hydrate on sediment
734 physical properties and fluid flow: a review. Geofluids, 3(4), 275-289.

735 Chand, S., Minshull, T. A., Gei, D., & Carcione, J. M. (2004). Elastic velocity models for gas-hydrate-
736 bearing sediments—A comparison. Geophysical Journal International, 159(2), 573-590.

737 Chand, S., Rise, L., Ottesen, D., Dolan, M.F.J., Bellec, V., Bøe, R., 2009. Pockmark-like depressions near
738 the Goliat hydrocarbon field , Barents Sea : Morphology and genesis 26, 1035–1042.
739 https://doi.org/10.1016/j.marpetgeo.2008.09.002

740 Collett, T., Bahk, J.., Boswell, R., Divins, D., Frye, M., Goldberg, D., Husebo, J., Koh, C.A., Malone, M.,
741 Myres, G., Shipp, C., Torres, M., 2014. Methane Hydrates in Nature- Current Knowledge and
742 Challenges. J. Chem. Eng. Data 60, 319–329.

743 Collett, T., Riedel, M., Cochran, J. R., Boswell, R., Kumar, P., & Sathe, A. V. (2008). Indian continental
744 margin gas hydrate prospects: results of the Indian National Gas Hydrate Program (NGHP)
745 expedition 01.

746 Cunningham, R., Lindholm, R.M., 2000. Seismic Evidence for Widespread Gas Hydrate Formation ,
747 Offshore West Africa 2000.

748 Dai, S., Santamarina, J.C., Waite, W.F., Kneafsey, T.J., 2012. Hydrate morphology: Physical properties
749 of sands with patchy hydrate saturation. J. Geophys. Res. B Solid Earth 117.
750 https://doi.org/10.1029/2012JB009667

751 Damuth, J. E. (1994). Neogene gravity tectonics and depositional processes on the deep Niger Delta
752 continental margin. Marine and Petroleum Geology, 11(3), 320-346.

753 Dewangan, P., Ramprasad, T., Ramana, M. V., Mazumdar, A., Desa, M., & Badesab, F. K. (2010).
754 Seabed morphology and gas venting features in the continental slope region of Krishna–
755 Godavari basin, Bay of Bengal: implications in gas-hydrate exploration. Marine and Petroleum
756 Geology, 27(7), 1628-1641.

757 Freudenthal, T., Wefer, G., 2015. Drilling cores on the sea floor with the remote-controlled sea floor
758 drilling rig MeBo. https://doi.org/10.5194/gi-2-329-2013

759 Freudenthal, T., Wefer, G., 2007. Scientific Drilling with the Sea Floor Drill Rig MeBo 63–66.
760 https://doi.org/10.2204/iodp.sd.5.11.2007

761 George, R.A.T., Cauquil, E., 2007. AUV Ultrahigh-Resolution 3D Seismic Technique for Detailed
762 Subsurface Investigations, in: Offshore Technology Conference. Houston, Texas, pp. 1–9.

763 Ghosh, R., Sain, K., Ojha, M., 2010. Effective medium modeling of gas hydrate-filled fractures using
764 the sonic log in the Krishna-Godavari basin, offshore eastern India. J. Geophys. Res. Solid Earth
765 115, 1–15. https://doi.org/10.1029/2009JB006711.

766 Guerin, G., Goldberg, D., & Meltser, A. (1999). Characterization of in situ elastic properties of gas

767 hydrate-bearing sediments on the Blake Ridge. Journal of Geophysical Research: Solid Earth,
768 104(B8), 17781-17795.

769 Gullapalli, S., Dewangan, P., Kumar, A., Dakara, G., & Mishra, C. K. (2019). Seismic evidence of free
770 gas migration through the gas hydrate stability zone (GHSZ) and active methane seep in
771 Krishna-Godavari offshore basin. Marine and Petroleum Geology, 110, 695-705.

772 Helgerud, M.B., Dvorkin, J., Nur, A., Sakai, A., Collett, T., 1999. Elastic wave velocity in marine
773 sediments with gas hydrates: Effective medium modeling 26, 2021–2024.

774 Helgerud, M.B., Waite, W.F., Kirby, S.H., Nur, A., 2009. Elastic wave speeds and moduli in
775 polycrystalline ice Ih, si methane hydrate, and sll methane-ethane hydrate. J. Geophys. Res.
776 Solid Earth 114, 1–11. https://doi.org/10.1029/2008JB006132

777 Holland, M., Schultheiss, P., Roberts, J., Druce, M., 2008. Observed Gas Hydrate Morphologies in
778 Marine Sediments. Icgh2008.

779 Hovland, M., Svensen, H., 2006. Submarine pingoes : Indicators of shallow gas hydrates in a
780 pockmark at Nyegga , Norwegian Sea 228. Marine Geology. 15–23.
781 https://doi.org/10.1016/j.margeo.2005.12.005

782 Jang, J., Santamarina, J.C., 2016. Hydrate bearing clayey sediments: Formation and gas production
783 concepts. Mar. Pet. Geol. 77, 235–246. https://doi.org/10.1016/j.marpetgeo.2016.06.013

784 Joshi, A.K., Sain, K., Pandey, L., 2018. Gas hydrate saturation and reservoir characterization at sites
785 NGHP-02-17 and NGHP-02-19 , Krishna Godavari Basin , eastern margin of India. Mar. Pet. Geol.
786 https://doi.org/10.1016/j.marpetgeo.2018.06.023

787 Judd, A., & Hovland, M. (2009). Seabed fluid flow: the impact on geology, biology and the marine
788 environment. Cambridge University Press.

789 Ker, S., Gonidec, Y. Le, Gibert, D., 2012. Multiscale seismic attributes: source-corrected wavelet
790 response and application to high-resolution seismic data. Geophys. J. Int. 190, 1746–1760.

Kim, H. S., Riedel, M., Ryu, B. J., Kim, G. Y., & Bahk, J. J. (2013). Improving gas hydrate saturation estimates using P-wave velocity log data by incorporating XRD-Data for detailed matrix-mineralogy definition. Marine and Petroleum Geology, 47, 155-167.

Kvenvolden, K.A., 1993. Gas hydrates - Geological perspective and global change. Rev. Geophys. 173–187.

Kumar, J., Sain, K., & Arun, K. P. (2019). Seismic attributes for characterizing gas hydrates: a study from the Mahanadi offshore, India. Marine Geophysical Research, 40(1), 73-86.

Malinverno, A., Kastner, M., Torres, M.E., Wortmann, U.G., 2008. Gas hydrate occurrence from pore water chlorinity and downhole logs in a transect across the northern Cascadia margin (Integrated Ocean Drilling Program Expedition 311). J. Geophys. Res. Solid Earth 113, 1–18. https://doi.org/10.1029/2008JB005702

Marsset, T., Marsset, B., Ker, S., Thomas, Y., Gall, Y. Le, 2010. Deep-Sea Research I High and very high resolution deep-towed seismic system : Performance and examples from deep water Geohazard studies 57, 628–637. https://doi.org/10.1016/j.dsr.2010.01.001

Marsset, T., Ruffine, L., Gay, A., Ker, S., E., C., 2018. Types of fluid-related features controlled by sedimentary cycles and fault network in deepwater Nigeria 89, 330–349. https://doi.org/10.1016/j.marpetgeo.2017.10.004

Riboulot, V., Sultan, N., Imbert, P., Ker, S., 2016. Initiation of gas-hydrate pockmark in deep-water Nigeria : Geo-mechanical analysis and modelling. Earth Planet. Sci. Lett. 434, 252–263.

Riedel, M., Collett, T.S., Hyndman, R.D., 2005. GEOLOGICAL SURVEY OF CANADA OPEN FILE 4934 Gas hydrate concentration estimates from chlorinity , e lectrical resistivity and seismic velocity GEOLOGICAL SURVEY OF CANADA OPEN FILE 4934 Gas hydrate concentration estimates from chlorinity , electrical resistivity and seismic velocity.

Riedel, M., Willoughby, E.C., Chen, M.A., He, T., Novosel, I., Schwalenberg, K., Hyndman, R.D.,

Spence, G.D., Chapman, N.R., Edwards, R.N., 2006. Gas hydrate on the northern Cascadia margin : regional geophysics and structural framework 311, 1–28. https://doi.org/10.2204/iodp.proc.311.109.2006

Sahling, H., Bohrmann, G., Spiess, V., Bialas, J., Breitzke, M., Ivanov, M., Kasten, S., Krastel, S., Schneider, R., 2008. Pockmarks in the Northern Congo Fan area , SW Africa : Complex seafloor features shaped by fluid flow 249, 206–225. https://doi.org/10.1016/j.margeo.2007.11.010

Shankar, U., Gupta, D.K., Bhowmick, D., Sain, K., 2013. Gas hydrate and free gas saturations using rock physics modelling at site NGHP-01-05 and 07 in the Krishna-Godavari Basin, eastern Indian margin. J. Pet. Sci. Eng. 106, 62–70. https://doi.org/10.1016/j.petrol.2013.04.004

Sloan, E.D., 1998. Gas Hydrates : Review of Physical / Chemical Properties 0624, 191–196.

Sultan, N., Bohrmann, G., Ruffine, L., Pape, T., Riboulot, V., Colliat, J.L., Prunele, A.D., Dennielou, B., Garziglia, S., Himmler, T., Marsset, T., Peters, C. a., Rabiu, a., Wei, J., 2014. Journal of Geophysical Research : Solid Earth. J. Geophys. Res. Earth 119, 2679–2694. https://doi.org/10.1029/2010JB007453.Pockmark

Sultan, N., Garziglia, S., Ruffine, L., 2016. New insights into the transport processes controlling the sulfate-methane-transition-zone near methane vents. Sci. Rep. 6, 1–9. https://doi.org/10.1038/srep26701

Sultan, N., Marsset, B., Ker, S., Marsset, T., Voisset, M., Vernant, A.M., Bayon, G., Cauquil, E., Adamy, J., Colliat, J.L., Drapeau, D., 2010. Hydrate dissolution as a potential mechanism for pockmark formation in the Niger delta. J. Geophys. Res. Solid Earth 115, 1–33. https://doi.org/10.1029/2010JB007453

Sultan, N., Voisset, M., Marsset, T., Vernant, A. M., Cauquil, E., Colliat, J. L., & Curinier, V., 2007. Detection of free gas and gas hydrate based on 3D seismic data and cone penetration testing: An example from the Nigerian Continental Slope. *Marine Geology*, *240*(1-4), 235-255.

Taleb, F., Garziglia, S., Sultan, N., 2018. Journal of Geophysical Research : Solid Earth

840 Hydromechanical Properties of Gas Hydrate-Bearing Fine Sediments From In Situ Testing
841 Journal of Geophysical Research : Solid Earth 9615–9634.
842 https://doi.org/10.1029/2018JB015824

843 Torres, M.E., Wallmann, K., Tre, A.M., Bohrmann, G., Borowski, W.S., Tomaru, H., 2004. Gas hydrate
844 growth , methane transport , and chloride enrichment at the southern summit of Hydrate Ridge
845 , Cascadia margin off Oregon 226, 225–241. https://doi.org/10.1016/j.epsl.2004.07.029

846 Ussler III, W., & Paull, C. K., 2001. Ion exclusion associated with marine gas hydrate deposits.
847 Washington DC American Geophysical Union Geophysical Monograph Series, 124, 41-51.

848 Vaular, E.N., Barth, T., Haflidason, H., 2010. Organic Geochemistry The geochemical characteristics of
849 the hydrate-bound gases from the Nyegga pockmark field , Norwegian Sea. Org. Geochem. 41,
850 437–444. https://doi.org/10.1016/j.orggeochem.2010.02.005

851 Waite, W.F., Santamarina, J.C., Cortes, D.D., Dugan, B., Espinoza, D.N., Germaine, J., Jang, J., Jung,
852 J.W., Kneafsey, T.J., Shin, H., Soga, K., Winters, W.J., 2009. PHYSICAL PROPERTIES OF HYDRATE-
853 BEARING SEDIMENTS 1–38. https://doi.org/10.1029/2008RG000279.

854 Wang, X., Hutchinson, D. R., Wu, S., Yang, S., & Guo, Y. (2011). Elevated gas hydrate saturation within
855 silt and silty clay sediments in the Shenhu area, South China Sea. Journal of Geophysical
856 Research: Solid Earth, 116(B5).

857 Wei, J., Pape, T., Sultan, N., Colliat, J.L., Himmler, T., Ruffine, L., de Prunelé, A., Dennielou, B.,
858 Garziglia, S., Marsset, T., Peters, C.A., Rabiu, A., Bohrmann, G., 2015. Gas hydrate distributions
859 in sediments of pockmarks from the Nigerian margin - Results and interpretation from shallow
860 drilling. Mar. Pet. Geol. 59, 359–370. https://doi.org/10.1016/j.marpetgeo.2014.09.013

861 Wood, W. T., Gettrust, J. F., Chapman, N. R., Spence, G. D., & Hyndman, R. D. (2002). Decreased
862 stability of methane hydrates in marine sediments owing to phase-boundary roughness.
863 Nature, 420(6916), 656.

Appendix A – Petrophysical Model

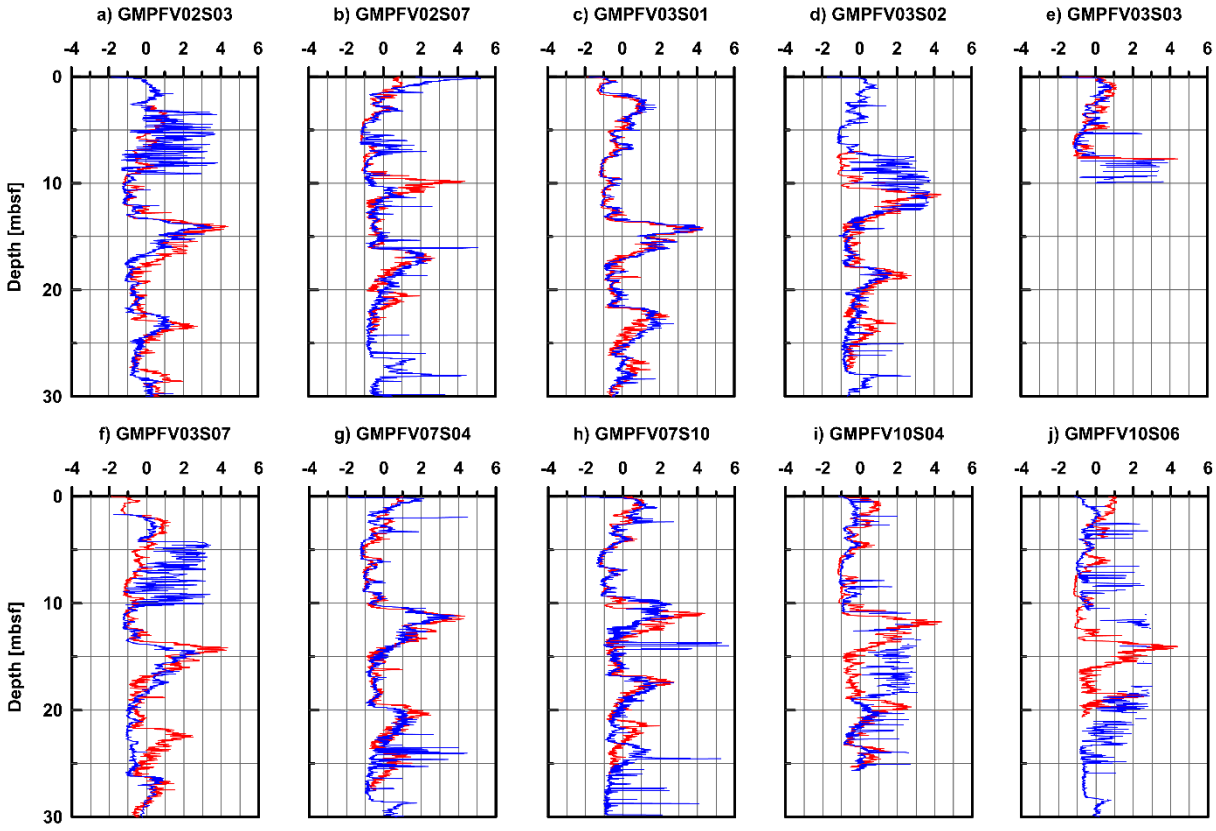


Figure A. Correlations between attenuations of compressional waves at reference site (red profiles) and GH bearing sites (blue profiles): a) GMPFV02S03, b) GMPFV02S07, c) GMPFV03S01, d)GMPFV03S02, e) GMPFV03S03, f) GMPFV03S07, g) GMPFV07S04, h) GMPFV07S10,i) GMPFV10S04, j) GMPFV10S06

Figure A shows correlations between attenuation profiles of compressional waves from GH bearing sediments (blue profiles) and those from reference sites (red profiles). Depth corrections between both profiles have allowed determining new depth-adjusted attenuation profiles at GH bearing sites; and, eventually use these profiles to define the mineral proportions needed in order to estimat GH content (see section 4: Mineralogy analysis).

Appendix B – Assumptions made in order to apply the effective medium theory

Assumptions and correlations were carried out throughout this work in order to apply the EMT. The following critical parametric study aims to quantify the error resulting from this process; thus, two uncertainties are discussed: a) the assumed constant value of the quartz profile and b) the assumed values of C_c and e_0 values. The residual error is calculated using the following equation:

$$Residual\ error\ = \ln \frac{x_{assumed}}{x_{actual}} \quad (8)$$

a) Mineralogy profile (assumed constant value of quartz)

After defining the calcite fractions, the quartz quantity was assumed constant with depth and equal to the average value of the quartz fraction at reference site. This allowed defining the clay fraction using equation 3.

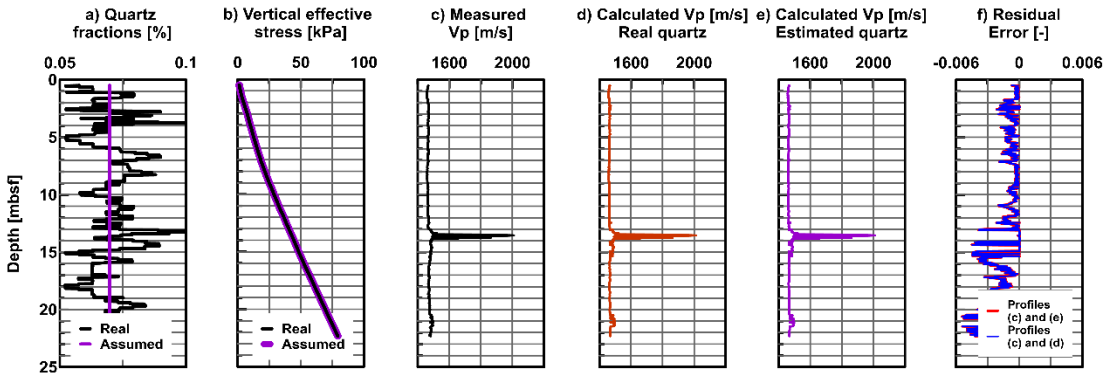


Figure B1. Parametric study accounting for the constant quartz assumption: a) measured and averaged quartz profiles from core GMCS05, b) vertical effective stress profile using the measured and averaged quartz value, c) Measured P-wave velocity at reference site GMPFV07S01, d) Calculated P-wave velocity using measured quartz value, e) Calculated P-wave velocity using averaged quartz value, f) residual error between measured and calculated P-wave velocity using measured quartz value and between measured and calculated P-wave velocity using averaged quartz value.

b) Density profile (assumed C_c and e_0 values)

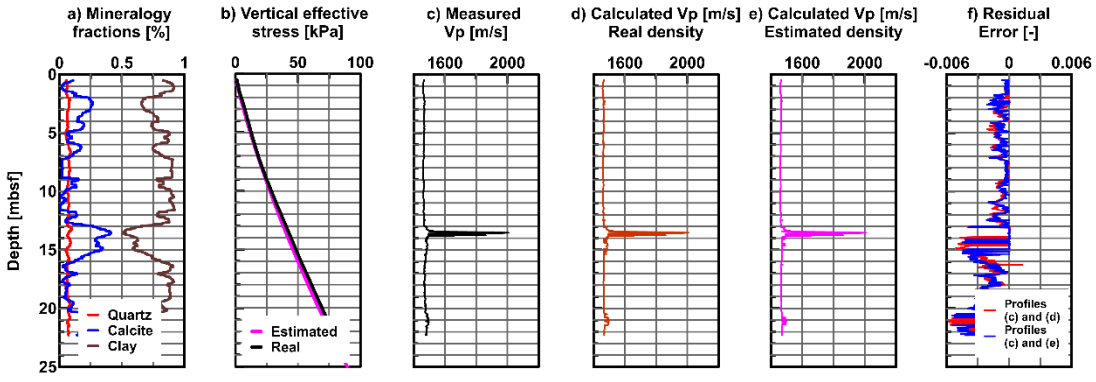


Figure B2. Parametric study accounting for assumed C_c and e_0 values: a) Mineralogy fractions from core GMCS05, b) vertical effective stress profile using real and assumed C_c and e_0 values, c) Measured P-wave velocity at reference site GMPFV07S01, d) Calculated P-wave velocity using real C_c and e_0 values, e) Calculated P-wave velocity using estimated C_c and e_0 values, f) residual error between measured and calculated P-wave velocity using real C_c and e_0 values and between measured and calculated P-wave velocity using assumed C_c and e_0 values.